A Proof-of-Concept OpenSim Moco Framework for Predictive Modelling of Passive Back-Support Exoskeletons

Master Thesis Biomedical Engineering
Alette R. van der Vlugt

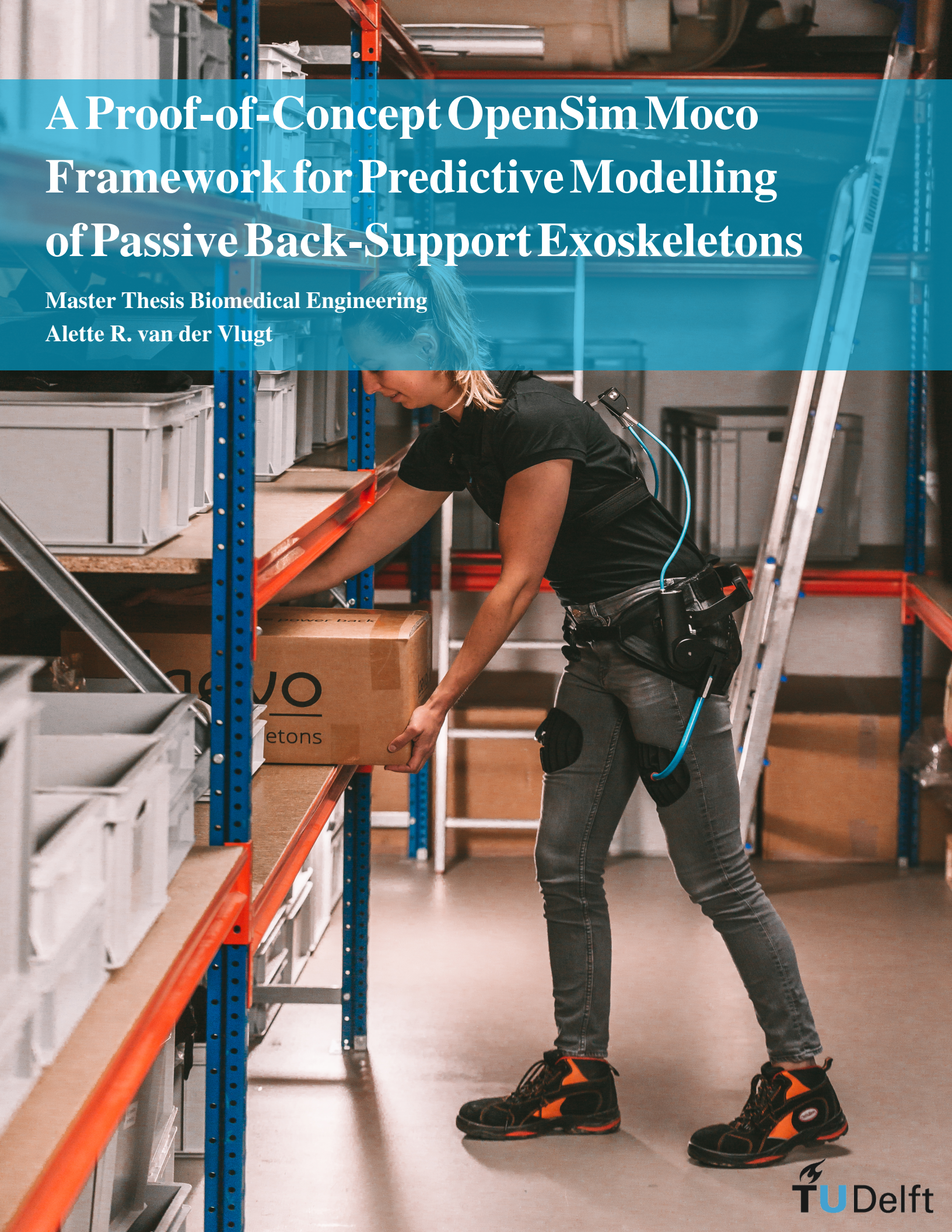

TU Delft

A Proof-of-Concept OpenSim Moco Framework for Predictive Modelling of Passive Back-Support Exoskeletons

Alette R. van der Vlugt
student number: 5594782

in partial fulfilment of the requirements for the degree of

Master of Science

in Biomedical Engineering

Track: Neuromusculoskeletal Biomechanics

at the Delft University of Technology,
to be defended publicly on Monday, July 6th, 2026 at 12:45.

Thesis advisors:	Dr. Ir. Arno Stienen Prof. Anne K. Silverman
Thesis committee:	Dr. Ir. Arno H.A. Stienen, Delft University of Technology, chair Prof. Anne K. Silverman, Delft University of Technology and Colorado School of Mines Dr. Ir. Eline van der Kruk, Delft University of Technology Dr. Ir. Laura Marchal Crespo, Delft University of Technology

An electronic version of this thesis is available at:
http://repository.tudelft.nl/

A Proof-of-Concept OpenSim Moco Framework for Predictive Modelling of Passive Back-Support Exoskeletons

Author: Alette van der Vlugt

***Abstract*—Back-support exoskeletons may reduce physical loading during lifting and stooping, but their effects are usually assessed indirectly using EMG and motion capture because individual muscle forces cannot be measured in vivo. This thesis developed and evaluated a proof-of-concept OpenSim Moco musculoskeletal modelling predictive simulation framework to estimate how a passive back-support exoskeleton affects muscle forces during stooping.**

Experimental data from nine healthy participants performing stoop-lifting trials with and without the passive rigid Laevo exoskeleton included synchronised EMG and motion capture. Analyses examined erector spinae activation, marker-based movement proxies, and hip and leg muscle activation. To determine significance, paired-sample t-tests were used. In OpenSim, the Laevo was modelled as a passive angle-dependent hip flexion torsional spring.

The experimental results did not show a statistically significant reduction in erector spinae activation when using the Laevo, for either peak activation ($p = 0.948$) or average activation ($p = 0.370$). The shoulder-hip distance results suggested a trend towards a smaller motion range when using the Laevo, especially in the empty-crate condition ($p = 0.090$), but this did not reach statistical significance. Clear statistical evidence for a general change in hip or leg muscle activation was not found, although average biceps femoris activation was significantly lower with the Laevo, decreasing from 0.563 to 0.484 in normalized activation ($p = 0.016$). The model showed partial qualitative agreement with some experimental trends, especially for selected movement-pattern and muscle-activation outcomes.

Overall, the developed framework generated predictive simulations with and without exoskeleton support. However, the results should be interpreted as a preliminary proof of concept rather than model validation. The main contribution is a reproducible OpenSim Moco workflow for modelling a passive back-support exoskeleton and comparing it with experimental EMG and motion-capture trends.

***Index Terms*—OpenSim Moco, back-support exoskeleton, musculoskeletal modelling**

I. Introduction

Worldwide, 1.71 billion people have a musculoskeletal condition, as stated by the WHO on the 14th of July, 2022. Musculoskeletal conditions are therefore the leading contributor to disability, with "low back pain the single leading cause of disability in 160 countries" [1]. In 2020, 619 million people were affected by low back pain, a number that is predicted to grow to 843 million people by 2050 [2]. In about 90% of the cases, low back pain is non-specific, meaning it cannot be attributed to a specific underlying diagnosis. Relevant risk factors include low physical activity and high physical stress at work [2]. In occupational-health literature, such physical stress is often discussed in relation to work-related musculoskeletal disorders, where work tasks contribute to the development of musculoskeletal problems. Risk factors at work include handling loads, especially when combined with bending, twisting, or awkward postures [3], [4]. Such tasks are common for employees in, for example, construction [5] or logistics and warehousing [6].

To reduce physical loading associated with low back pain risk, a proposed intervention is the use of back-support exoskeletons. Exoskeletons are assistive devices that are worn by the user and designed to support the body during physical tasks. Back-support exoskeletons specifically provide support to the back or lower back, commonly by assisting trunk or hip extension during tasks such as lifting, bending, or stooping [7]. Structurally, two main types of exoskeletons are commonly recognised: rigid exoskeletons and soft exosuits. Rigid exoskeletons use rigid components, while soft exosuits often use textile structures and elastic elements such as elastic bands to transmit forces [7]. Both types can be further classified as either active or passive. Active exoskeletons use powered actuation, often involving control systems and an energy source such as a battery, whereas passive exoskeletons provide support through mechanical elements without powered actuation [7].

Current evidence on the effects of back-support exoskeleton use is mainly based on biomechanical research in laboratory experiments. However, biomechanical research is limited by practical constraints, such as the inability to directly measure individual muscle forces in vivo [8], [9]. The research is further complicated by the high biomechanical redundancy of the human body [10], since the same movement or posture can be produced by different combinations of muscle activations and muscle forces. As individual muscle forces cannot be measured directly in vivo, studies commonly rely on indirect measures to assess the effects of exoskeletons. For example, surface EMG was used in 33 out of 42 studies reviewed by [11], while motion capture was used in 18 out of 42 studies. These measures can be used as proxies for the effects of an exoskeleton by comparing conditions with and without using an exoskeleton.

The experimental part of this thesis will use both EMG and motion capture. The exoskeleton that will be studied is a passive rigid exoskeleton, the Laevo Flex. The intention of the exoskeleton is to unload the back, often studied via the proxy of back muscle activation, since load shifts cannot be

measured directly using surface EMG. With this proxy, a lower activation is seen as unloading of the back. In previous studies, back muscle activation is commonly reported to decrease when using a back-support exoskeleton, for example during forward leaning [12]. Therefore, the first hypothesis of this thesis is that the use of a back-support exoskeleton decreases the activation of the back muscles.

However, using an exoskeleton may prompt the user to alter their movement strategy. For example, Luger et al. [13] found that using an exoskeleton may affect trunk posture, back inclination, or knee flexion. This thesis will study if users use altered movement patterns by looking at a proxy for back flexion and knee flexion, since these are practically the easiest to measure. Since [13] found movement changes, the second hypothesis is that the use of a back-support exoskeleton changes back or knee motion during stooping.

An altered motion pattern may result in a redistribution of muscle demand, which is related to the load shifts reported by [14], including shifts from the shoulder to the lower back and from the lower back to the knee. This means that, even if the back muscles are unloaded, the biomechanical demand as a whole may not decrease and could even increase elsewhere. To investigate whether such a redistribution occurred, this thesis examines the activation of one hip muscle, the gluteus medius, and two leg muscles: the biceps femoris, a knee flexor and hip extensor, and the rectus femoris, a knee extensor and hip flexor. The third hypothesis is therefore that the use of a back-support exoskeleton changes hip or leg muscle activation.

To address some of the limitations of experiments including the infeasibility of measuring individual muscle forces, musculoskeletal modelling is an increasingly used approach. This computational approach can help estimate what is happening inside the body, without the need for invasive measurements [15]. Musculoskeletal models generally represent the skeleton as rigid body segments connected by joints, with muscles or muscle-tendon units acting across these joints. More detailed neuromusculoskeletal models may also include aspects of neural control, but these are outside the scope of this thesis. Multiple musculoskeletal modelling programs exist, with AnyBody [16] and OpenSim [15], [17] being two well-known examples. The focus of this thesis is OpenSim, because it is open-source, user-extensible, widely used in academic musculoskeletal modelling, and compatible with OpenSim Moco, capable of predictive modelling [15], [18]. This is relevant because the focus of this thesis will be on predictive modelling. In inverse modelling, experimentally measured motion is used as input to a model and used to estimate quantities such as joint moments, muscle forces, or joint reaction forces. In predictive modelling, also referred to as forward dynamics, the motion is not prescribed beforehand, but predicted based on model dynamics, constraints, and an objective function. OpenSim Moco is suitable for this because it can be used to solve musculoskeletal optimal-control problems, including motion prediction and parameter optimisation [18].

Predictive modelling in general, and OpenSim Moco specifically, has successfully been used in gait-related studies and assistive-device applications, showing that musculoskeletal optimal control can be applied to human-device interaction problems [18], [19]. However, its application to occupational back-support exoskeletons and non-gait tasks such as forward stooping remains limited. Challenges in back-support exoskeletons include the larger number of muscles and degrees of freedom compared to the lower limbs, resulting in a more complex model and a higher difficulty to reach convergence. Therefore, the goal of this thesis is to develop a framework for predictive modelling of back-support exoskeletons using OpenSim Moco and to demonstrate its potential through a proof of concept.

As mentioned, predictive modelling is dependent on model dynamics, constraints, and the selected objective function. This thesis focuses on developing a proof of concept to demonstrate the possibilities of the proposed framework, rather than developing a clinical or directly predictive design tool. The proof of concept is limited to one passive rigid back-support exoskeleton, the Laevo, and one task, forward stooping. A generic full-body model of a healthy individual is used. To evaluate the plausibility of the proof of concept, predicted muscle activations and kinematics are compared with experimental results, based on the three previously discussed hypotheses.

The objectives of this thesis are therefore to: (1) develop an OpenSim Moco framework for modelling back-support exoskeletons; (2) apply this framework to a proof-of-concept task; (3) evaluate whether the model can predict changes in muscle activation and effort-related load indicators by comparing the results with experimental data; and (4) identify computational and modelling limitations. These objectives lead to the following contributions: (1) a reproducible framework for modelling a back-support exoskeleton in OpenSim Moco; (2) a proof of concept for forward stooping with a rigid back-support exoskeleton; and (3) insight into the feasibility and limitations of using predictive musculoskeletal modelling for back-support exoskeletons.

II. Methods

A. Experimental equipment

The experimental setup consisted of a Qualisys infrared motion capture system, a TMSi Porti7 8b8at system for EMG recording, and an Arduino-based synchronization system. The Arduino generated a pseudo-random binary sequence (PRBS) signal at 50 Hz using a digital output pin. This signal was simultaneously sent to the trigger input of the TMSi system and to an infrared LED visible to the motion capture system. The shared PRBS signal was used to synchronize the EMG and motion capture data during post-processing using cross-correlation, for more details, see Appendix A. The motion capture and EMG data were acquired at 250 Hz and 2048 Hz, respectively. A schematic of the experimental setup is shown in Figure 1.

During the stooping task, participants grasped a crate to make the movement more repeatable. The crate was equipped with eight infra-red reflective markers, with one marker placed

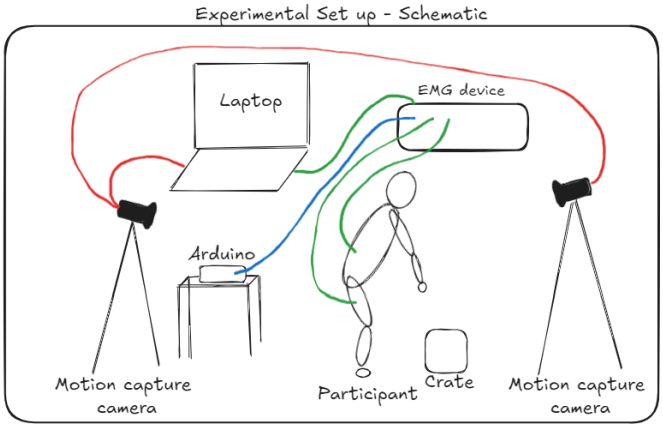

Fig. 1. Schematic overview of the experimental setup used to collect synchronized motion-capture and EMG data during stoop lifting. The figure shows the participant with EMG cables, the surrounding motion-capture cameras, and the Arduino-controlled infrared LED used to send the same PRBS trigger signal to both systems. This setup allowed the EMG and motion-capture recordings to be aligned during post-processing.

on each corner. This marker configuration allowed the crate to be tracked as a rigid body while maintaining sufficient marker visibility in case some markers were temporarily occluded.

B. Subjects and experimental procedure

Nine healthy subjects who had no prior experience with the exoskeleton participated in the study, five women and four men. The study was approved by the Human Research Ethics Committee (HREC) of TU Delft, and all participants provided vocal informed consent prior to participation.

Before the experimental trials, participants were instrumented with eight pairs of surface EMG electrodes and one ground electrode, which was placed on the neck, for a graphic overview on electrode locations and details on connection to the EMG setup see Appendix B. No specific skin preparation was performed before electrode placement, and the inter-electrode distance was not measured explicitly. EMG signals were recorded from six muscles on the left side only and from one muscle bilaterally. This side convention was chosen because of the available number of EMG channels. The erector spinae longissimus was measured bilaterally, while the erector spinae iliocostalis, external oblique, rectus abdominis, gluteus medius, biceps femoris, and rectus femoris were measured on the left side. The muscles were selected based on the hypotheses of this thesis, previous exoskeleton and lifting studies [12], [13], [20], [21], the expected involvement of back, hip, and leg muscles during stoop lifting and the need to avoid interference between the electrodes and the exoskeleton. Electrode placement followed the anatomical landmark descriptions from placement guides. Specifically, the external oblique and rectus abdominis placements were based on [22], while the remaining placements were based on [23].

After EMG instrumentation, participants were equipped with passive infrared markers for motion capture. The marker set was based on Riahi et al, [24], with adaptations due to practical limitations, including the available number of markers and marker clusters. The marker set consisted of a headband, two marker clusters on the lower legs, two markers on the medial and lateral side of each knee and ankle, one marker on each hip, one marker on each shoulder, one marker on each elbow, and two markers on each wrist. For a graphic overview see Appendix C.

Subsequently, two reference trials were recorded: a static trial in an anatomical standing position for motion-capture calibration and a resting trial for EMG baseline recording. After these reference trials, the stoop-lifting trials were performed in a fixed order. First, the participant performed the stoop lift without the exoskeleton using the empty crate, followed by the 5 kg crate. The exoskeleton was then put on over the EMG electrodes and markers, according to the instructions as can be found in Appendix D. Only the hip markers were removed and replaced on top of the exoskeleton; all other markers and all surface electrodes remained in place. The participant then performed the stoop lift with the empty crate and with the 5 kg crate while wearing the exoskeleton. The order was fixed to avoid repeated donning and doffing of the exoskeleton, which would have increased measurement time and could have displaced the electrodes and markers. Additional measurements were collected but were outside the scope of this thesis.

The exoskeleton used in this study was the rigid, passive Laevo Flex. It interacts with the user through pads on the proximal anterior thighs, a vest on the upper body, and a frame around the hips. The electrode and marker locations were chosen to avoid these interaction surfaces where possible, allowing the Laevo to be donned over the measurement setup. Electrode cables were routed with sufficient slack to reduce pulling during the stooping motion. For each participant, the Laevo was fitted according to the device guidelines, from Appendix D, mainly by tightening the straps and, when needed, changing the vest and the blue back-connection elements.

C. Experimental data processing

1) EMG processing: After synchronisation, the EMG data were processed offline in Python. All code used in this thesis can be found on github at https://github.com/Alette0012/master-thesis. The filtering procedure was based on [25], with adaptations because the TMSi Porti7 applied less online filtering than the device used in that study. The following processing steps were applied:

- High-pass filtering at 20 Hz using a fourth-order Butterworth filter with zero-phase filtering, to remove drift and movement artefacts from the cables and electrodes.
- Low-pass filtering at 500 Hz using a fourth-order Butterworth filter with zero-phase filtering, to remove high-frequency noise outside the relevant EMG bandwidth.
- Full-wave rectification by taking the absolute value of the filtered signal, to obtain a positive EMG amplitude signal.
- Low-pass filtering of the rectified signal at 2.5 Hz using a fourth-order Butterworth filter with zero-phase filtering, to obtain a smooth linear envelope representing muscle activation. This cut-off frequency was based on [12].

The final processed EMG signal used in the analysis was the linear envelope resulting after these filtering steps. For the muscle analysis, the EMG envelopes were amplitude-normalized within each participant and recording side by dividing them by a participant-specific 95th-percentile reference value computed from the valid lifting intervals. This part was therefore a within-participant normalization approach rather than MVC-based normalization, meaning the EMG results were primarily interpreted as relative changes in activation pattern. In addition, each lift was time-normalized to 0-100% of the crate-in-air phase.

2) Motion capture processing: The motion capture data were manually processed in Qualisys Track Manager. Markers were labelled where visible, although the final marker set differed slightly between participants due to marker occlusion and practical limitations during the measurements. The markers used for the present analysis included two shoulder markers, two hip markers, and two lateral knee and two lateral ankle markers. After labelling, the marker trajectories were exported as `.mat` files and further processed in Python.

The crate trajectory was derived from unidentified motion-capture marker trajectories. Candidate crate markers were selected from the most visible unidentified markers and grouped based on approximately rigid-body behaviour, quantified by low variation in pairwise inter-marker distances over time. From this cluster, the markers with the lowest median vertical positions were retained to represent the lower part of the crate. Depending on marker visibility, this resulted in three or four retained markers per trial. Crate height was then calculated as the mean vertical position of these retained markers, with missing samples linearly interpolated and the resulting signal smoothed. Lift intervals were identified from the smoothed crate-height signal using its vertical speed together with an estimated ground-contact level. Brief pauses between motion phases were merged, and only intervals exceeding a minimum duration were retained. Lift onset was defined as the last frame on the estimated ground-contact level before the motion phase, and lift end as the first frame returning to that ground-contact range after the motion phase.

Participant movement was described using marker-derived kinematic outcome measures. These measures were not intended to exactly reproduce the generalized coordinates of the OpenSim model, but were used to compare movement trends between the experimental conditions with and without the exoskeleton. The following outcome measures were extracted:

- Crate vertical displacement, calculated from the average vertical position of the retained crate markers. This measure was used to identify the lifting phase.
- Shoulder-to-hip distance, calculated as the distance between the shoulder and hip markers in the sagittal plane. This measure was used as a proxy for trunk flexion and stoop depth. More details and a graphic overview can be found in Appendix E.
- Knee flexion angle, calculated from the hip, knee, and ankle marker positions in the sagittal plane. For more details on the calculation and a graphic see Appendix F.

Because the predictive simulations were not driven by participant-specific marker trajectories but by a generic model, the experimental kinematic variables were compared with the simulated outputs only at the level of movement trends and condition-dependent differences. Therefore, the motion capture analysis was used to evaluate whether the exoskeleton affected the general movement strategy, rather than to perform direct coordinate-by-coordinate validation of the OpenSim simulation.

3) Statistical analysis: Experimental EMG comparisons were performed at the participant level between the no-exoskeleton and Laevo conditions, using only valid paired observations. For each participant, peak and mean values were extracted from the lift-averaged, time-normalized EMG profile. Two-sided paired-sample t-tests were used to test within-participant differences between conditions. For each outcome, the condition means, mean paired difference, test statistic, p-value, and Cohen's d_z effect size were reported. Because this study was designed as a feasibility study, sample-size estimates were also calculated for selected target effect sizes to indicate the number of paired participants that would be needed for more detailed statistical analysis in future work.

D. Musculoskeletal model

The predictive simulations were performed in OpenSim 4.5 with Moco 4.5.2, using the generic male full-body thoracolumbar spine model: `Male_Thoracolumbar_Spine_Model_FullBody_v2.0_OS4`, based on the thoracolumbar spine and rib cage model developed by Bruno et al. This model contains 111 degrees of freedom and 620 muscle-tendon actuators [26]. The model was selected because it includes a detailed thoracolumbar spine representation as well as the trunk, hip and lower-limb musculature required to simulate stooping motion.

The original model was modified to represent the simplified sagittal-plane stooping task used in the predictive simulations. A subset of the model joints and coordinates was retained, including the hip, knee, ankle, and selected thoracolumbar coordinates. Coordinates associated with out-of-plane motion, such as hip adduction and axial rotation, were constrained because the simulated movement was assumed to occur in the sagittal plane. The complete list of retained and constrained coordinates is provided in Appendix G. The predictive model was run for two different cases, one that included the hip and leg muscles, and the other with the back muscles. The list of included muscles, as well as a graphic overview of the included muscles can be found in Appendix G.

The calcaneus bodies of both feet of the model were welded to the ground. This represented the experimental condition in which participants remained approximately in place during the stooping task and prevented translation of the model relative to the ground. The model was not subject-specifically scaled, all simulations were therefore performed using the generic male model.

The original coordinate actuators in the model were removed since they actuated coordinates that were removed and

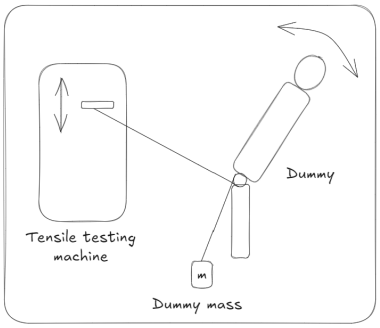

Fig. 2. Schematic overview of the mechanical dummy setup used to measure the Laevo angle-torque relationship. The Laevo was mounted on a dummy with a rotating trunk, and a tensile testing machine applied motion through a pulley-cable system. This setup allowed the measured force and displacement to be converted into an exoskeleton support torque as a function of flexion angle.

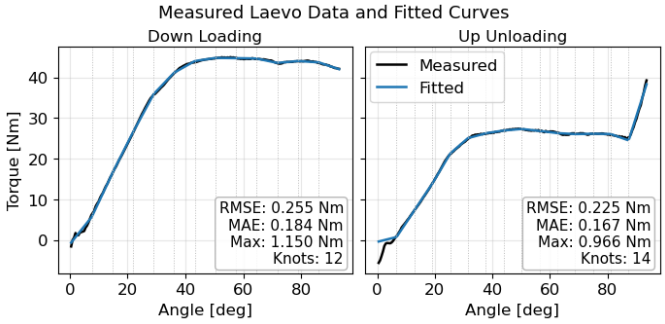

Fig. 3. Measured and fitted Laevo angle-torque relationships for the loading and unloading motions. The measured curves show the experimentally derived support torque after correction for the gravity-only test setup, while the fitted curves show the smoothed piecewise linear approximations used in OpenSim. The separate motions show the hysteresis in the Laevo response and were used for the stooping and standing-up simulations, respectively.

replaced by coordinate actuators on the retained coordinates. These actuators were included to support numerical convergence of the predictive simulations, but have no biological meaning. In the final simulations, the reserve actuators were progressively weakened and penalized to reduce their contribution relative to the muscle actuators. The final reserve actuator settings and the retained muscle set are provided in Appendix G.

E. Derivation and implementation of the Laevo support torque

The Laevo was represented in OpenSim as a passive angle-dependent support torque. This choice was based on the models built by Riahi et al. [24]. Because the manufacturer-provided support characteristic was not available in a form suitable for direct modelling, the relationship between exoskeleton angle and support torque was derived experimentally. The measurement procedure and data processing are described in detail in Appendix H. In brief, the Laevo was mounted on a mechanical dummy and tested using a tensile testing machine, see a schematic view in Figure 2. The measured force and displacement were converted to torque and flexion angle using the pulley geometry. Gravity-only measurements of the dummy and test setup were processed in the same way and subtracted from the Laevo measurements to isolate the exoskeleton contribution. The resulting relationship was retained as separate loading and unloading branches, because the measurements showed hysteresis.

The processed angle-torque curves were then implemented in OpenSim using `ExpressionBasedCoordinateForce` components on the hip flexion coordinates, as described in Appendix I. This was chosen as a simplified initial implementation and means that the modelled device does not implement the interaction on the upper leg, chest and hip as the Laevo does in reality. Since this OpenSim force type requires a continuous analytical expression, the measured loading and unloading motions were approximated using smoothed piecewise linear spline expressions:

$$\tau_{\text{exo}}^{\text{side}}(q,\chi) = -\frac{1}{2}\,\phi\left(a_0^{(\chi)} + a_1^{(\chi)} q + \sum_{i=1}^{N_\chi} a_{i+1}^{(\chi)} \rho\Big(q - \kappa_i^{(\chi)}\Big)\right),$$
$$\rho(x) = \frac{1}{2}\left(x + \sqrt{x^2+\varepsilon^2}\right),$$
$$\phi(x) = \frac{1}{2}\left(x + \sqrt{x^2+\delta^2}\right), \tag{1}$$

where q is the hip flexion angle, χ denotes the loading branch (*down*) or unloading branch (*up*), $\varepsilon = 8.72665 \times 10^{-3}$ rad, and $\delta = 0.25$ Nm. The fitted coefficient vectors $\mathbf{a}^{(\chi)}$ and knot locations $\boldsymbol{\kappa}^{(\chi)}$ are presented in Table VII in Appendix I. The fitted curves are shown in Figure 3. Separate expressions and therefore separate musculoskeletal models were used for stooping and standing-up simulations, corresponding to the loading and unloading motions, respectively. The measured torque was interpreted as the total bilateral support of the Laevo and was therefore divided equally over the left and right hip flexion coordinates. In this way, the combined exoskeleton moment applied in the musculoskeletal model corresponded to the experimentally derived whole-device support torque.

F. Predictive simulation setup with OpenSim Moco

Predictive simulations were performed using OpenSim Moco. The aim was to generate a sagittal-plane stooping and standing-up movement and to evaluate the effect of the implemented Laevo support torque on the resulting motion and muscle activity. Two model conditions were simulated: one without Laevo support and one with Laevo support. To reduce computation time, all muscle-driven simulations were run on the DelftBlue supercomputer [27]. No external crate load was included in the predictive simulations.

The simulations were formulated as `MocoStudy` problems. Each study consisted of a `MocoProblem`, in which the model, state bounds, control bounds, endpoint constraints, path constraints, and cost terms were defined, and a `MocoSolver`, which solved the resulting optimal-control problem. The prob-

lem optimized the model states and controls while satisfying the musculoskeletal dynamics and imposed constraints [18].

The complete movement was divided into two phases that were solved separately: a stooping phase and a standing-up phase. The stooping phase started from an upright standing posture, defined by setting the retained joint angles to zero and imposing zero initial speeds. The final state of the stooping phase was defined using an endpoint constraint on shoulder height and zero values for final speeds. To be able to set this endpoint constraint, a shoulder reference point was required. This point was set to be the origin of the humerus frame, and its vertical position in the ground frame was constrained to reach 0.25 ± 0.05 m. This target was selected through pilot tuning to obtain a deep stooping posture while maintaining convergence of the optimization problem.

The standing-up phase started from the final posture of the stooping phase with initial speeds zero and ended in the upright standing posture. The final state was defined by setting the retained joint angles and speeds to zero. The loading branch of the Laevo torque-angle relationship was used for the stooping phase, while the unloading branch was used for the standing-up phase.

The cost function included a final-time goal and a control-effort goal. The final-time goal had a weight of 0.1, and the control-effort goal had a weight of 1. The duration of the stooping phase was bounded between 0.8 and 1.2 s, while the duration of the standing-up phase was bounded between 1.1 and 1.6 s. Muscle excitations and activations were bounded between 0 and 1.

To enforce bilateral sagittal-plane motion, symmetry constraints were imposed on the left and right hip flexion, knee flexion, and ankle plantar/dorsiflexion coordinates throughout the trajectory. These constraints were included because the simulated task was assumed to be symmetric and restricted to the sagittal plane. Coordinate and speed bounds for the retained model coordinates are provided in Appendix G.

G. Predictive simulation procedure

All predictive simulations were run in Python using OpenSim 4.5 [15], [17] and OpenSim Moco 4.5.2 [15], [18]. The Moco problems were solved using `MocoCasADiSolver`. The solver used 25 mesh intervals, a convergence tolerance of 10^{-1}, a constraint tolerance of 10^{-2}, and a maximum of 40,000 iterations. The transcription scheme was not set explicitly, so the default `MocoCasADiSolver` setting was used.

A continuation strategy was used to improve convergence of the muscle-driven predictive simulations, see Table I. First, an actuator-only version of the model was solved using coordinate actuators with the optimal force parameter set to 200 Nm. The unit of the optimal force parameter for a rotational actuator is Nm, and represents the maximum torque it can deliver for a maximum actuation, which has a unitless value of 1.0. This solution was used as an initial guess for subsequent simulations. In the next step, the selected muscles were added to the model while retaining the reserve actuators. The reserve actuator settings were then progressively adjusted, reducing their strength and increasing the penalty. Once the run with the no-exoskeleton solved within the set standards, that run was used as a seed for the exoskeleton run, without any other changes.

Four simulation setups were used: a stooping and standing-up phase for the hip and leg muscle model, and a stooping and standing-up phase for the back muscle model. For the hip and leg muscle simulations, a maximum reserve actuator torque of 1 Nm was considered acceptable. For the back-muscle simulations, this reserve actuator limit could not be reached while maintaining convergence. Therefore, higher reserve actuator torques were accepted, provided that the constraint violation remained below the selected tolerance. These simulations were therefore used only to explore qualitative trends.

TABLE I
CONTINUATION STRATEGY USED TO OBTAIN THE FINAL MUSCLE-DRIVEN PREDICTIVE SIMULATION FOR THE HIP AND KNEE SIMULATION.

Step	Model configuration	Reserve actuator settings	Purpose
1	Actuator-only model	200 Nm optimal force	Obtain feasible initial guess
2	Muscles added	200 Nm optimal force; hip/knee penalty 5	Introduce muscle actuation
3	Muscles + reduced reserves	Hip/knee optimal force 50 Nm; penalty 15	Reduce reserve contribution
4	Final model	Hip 5 Nm, knee 15 Nm; hip penalty 50, knee penalty 5	Final predictive solution

H. Simulation data processing

The Moco solutions were exported as `.sto` files and processed in Python. For each simulation, the coordinate trajectories, muscle excitations, muscle activations, and reserve actuator controls were extracted where available. The coordinate trajectories were used to evaluate the predicted stooping and standing-up motion, including hip, knee, ankle, and thoracolumbar motion, as well as the achieved shoulder height.

III. RESULTS

A. Experimental results lifting patterns

After synchronisation with the PRBS signal and the other processing steps, the lifting periods could be isolated. Figure 4 shows the results of one trial, with the left and right erector spinae longissimus and the erector spinae iliocostalis. The grey shaded regions indicate the periods during which the crate was off the ground. At the start of each shaded region, the participant was stooped forward, around the middle of the shaded region, the crate was at its highest, and at the end, the crate was placed back on the ground. The muscle activation patterns aligned with the shaded regions, and the measured back muscles showed similar timing. In this example, the participant completed 10 identifiable lifts.

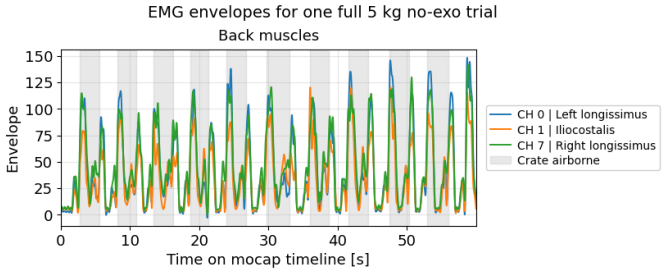

Fig. 4. Example of the processed EMG signals for one stoop-lifting trial, with grey shaded regions indicating the detected crate-in-air intervals, detected from the motion capture data. The back-muscle channels show repeated activation patterns aligned with the lifting intervals, supporting that the synchronisation and lift-detection procedure identified the relevant movement phases.

B. Effect of the Laevo on erector spinae activation

The first hypothesis stated that the Laevo would reduce back muscle activation during stoop lifting. This was evaluated by comparing the normalized erector spinae longissimus activation in the 5 kg crate condition with and without the Laevo for the experimental trials. Figure 5 shows the average experimental EMG signal for the valid trials at the top and the modelling results below.

The experimental plot shows a slight decrease in peak activation when using the Laevo, whereas average activation appears slightly higher. However, the paired comparisons using data of the five participants for whom valid data was available showed no significant difference between conditions for either peak activation (mean difference = -0.008, $t(4) = -0.070$, $p = 0.948$, $d_z = -0.031$) or average activation (mean difference = 0.041, $t(4) = 1.009$, $p = 0.370$, $d_z = 0.451$), as also presented in Table II.

The modelling results are shown in the bottom plot of Figure 5. All modelled back muscles showed a similar activation pattern, although the activation magnitude differed between muscles. Activation spiked at the start of the lifting cycle then dropped and rose to a peak, followed by a decrease to near zero around mid-cycle and a second peak near the end of the lifting cycle. The first-half peak was also visible in the experimental EMG signal, whereas the timing and presence of the second-half peak differed between the experimental and modelling results. In the experimental data, a small peak was visible around 80% of the lifting cycle for the Laevo condition, while this was not clearly present in the no-exoskeleton condition. In the model, the second peak occurred near the end of the lifting cycle for both the Laevo and no-exoskeleton conditions. The highest activation was found for IL L1 and LTpL L1, corresponding to the most cranial components of the modelled iliocostalis lumborum and longissimus thoracis pars lumborum muscle groups.

C. Effects in movement patterns

The second hypothesis stated that using the exoskeleton would change the user's motion. To evaluate this, the shoulder-hip distance and knee angle were derived from the motion-capture results and the modelling results.

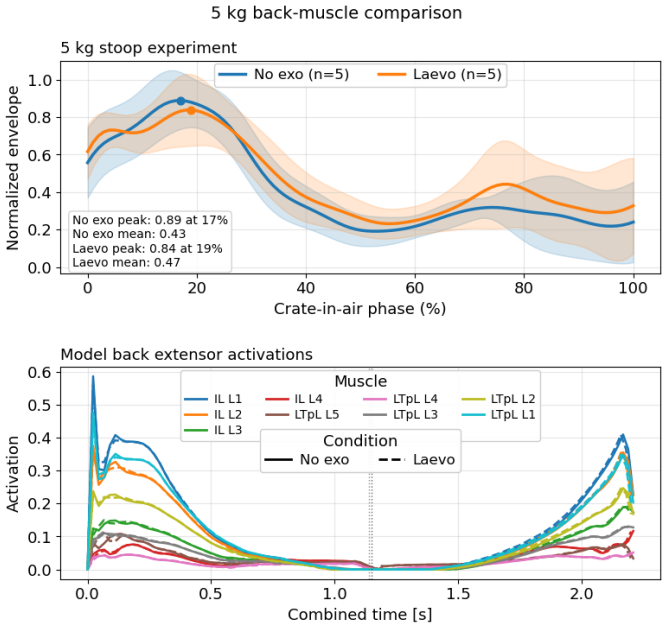

Fig. 5. The experimental and modelled back muscle activation plotted, with and without the Laevo during the 5 kg stoop-lifting condition. The experimental results show no clear reduction in normalized erector spinae activation with the Laevo, and the model similarly predicts only small differences between conditions. During the standing-up phase, in the first half of the movement, both the experimental and modelled activations are highest while the participant is stooped and decrease as the participant becomes upright. During the stooping phase, in the second half of the movement, both increase again as the participant bends forward to set the crate down, although the model differs from the experimental results in the detailed shape and timing of this increase.

TABLE II
PAIRED-SAMPLE T-TEST RESULTS FOR NORMALIZED ERECTOR SPINAE ACTIVATION IN THE 5 KG CRATE CONDITION WITH AND WITHOUT THE LAEVO. MEAN DIFFERENCES ARE CALCULATED AS LAEVO MINUS NO EXOSKELETON.

Measure	No exo	Laevo	Diff.	$t(4)$	p	d_z
Peak	0.934	0.926	-0.008	-0.070	0.948	-0.031
Average	0.427	0.467	0.041	1.009	0.370	0.451

The shoulder-hip distance range results are shown in Figure 6. This plot includes both the empty crate and 5 kg crate trials, since these load conditions were not compared against each other. The shoulder-hip distance was included as a marker-based outcome measure related to back flexion during the stoop. For all trials except one, the shoulder-hip distance range was smaller with the exoskeleton than without the exoskeleton. The participant-average results and the modelling results are shown in the leftmost and rightmost pairs of the plot, respectively.

Paired-sample t-tests were performed to compare the participant-average shoulder-hip distance range with and without the Laevo. For both load conditions, three paired participants were included. The results are shown in Table III. A trend towards a smaller shoulder-hip distance range with the Laevo was visible, but it did not reach statistical significance. This trend was strongest in the empty crate condition, where

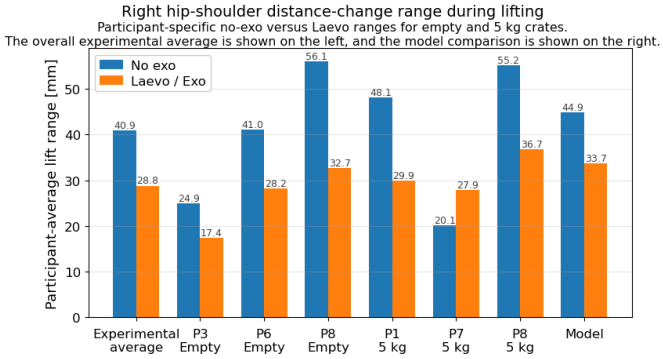

Fig. 6. Range of the shoulder-hip distance during the lifting movement, calculated as the difference between the largest and smallest sagittal-plane distance between the hip and shoulder markers. A smaller range indicates less flexion in the back. Most experimental trials and the model showed a smaller range with the Laevo, suggesting a possible reduction in trunk flexion range or a change in movement strategy.

TABLE III
PAIRED-SAMPLE T-TEST RESULTS FOR THE SHOULDER-HIP DISTANCE RANGE. MEAN DIFFERENCES ARE CALCULATED AS LAEVO MINUS NO EXOSKELETON. VALUES FOR NO EXO, LAEVO, AND DIFF. ARE IN MM.

Condition	No exo	Laevo	Diff.	t	p	dz
Empty	40.670	26.111	-14.559	-3.110	0.090	-1.795
5 kg	41.134	31.530	-9.604	-1.103	0.385	-0.637

the mean difference was -14.559 mm and the p-value was 0.090. The model results showed the same direction of change, with a smaller shoulder-hip distance range when the exoskeleton was included.

Figure 7 shows the knee-angle values calculated from the experimental marker data and extracted from the model. The shaded uncertainty regions in the experimental results overlap for a large part of the lifting movement, suggesting that the difference between the no-exoskeleton and Laevo conditions was small relative to the variation in the data. In contrast to the shoulder-hip distance, which was evaluated using a single value, the knee angle was evaluated over the full movement pattern. Therefore, no statistical test was performed on summary values.

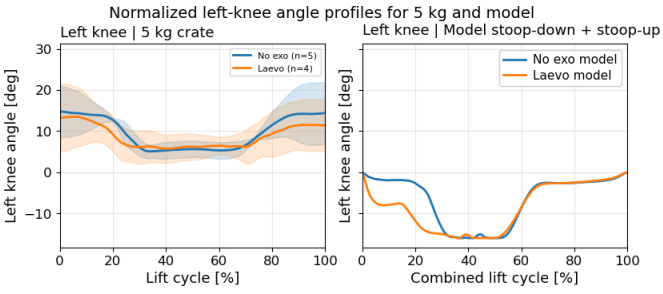

Fig. 7. Experimental knee-angle proxy and model knee angle over the normalized lifting movement. The experimental curves show overlapping uncertainty regions, indicating that the difference between conditions was small relative to the variation in the data. The model reproduced the general no-exoskeleton pattern of knee flexion in the stooped posture, extension during upward lifting, and renewed flexion during the downward phase, but showed only partial agreement with the experimental Laevo-related changes.

The experimental and model results showed a similar general knee-angle pattern in the no-exoskeleton condition, with the knee angle decreasing as the knees extended and increasing again later in the movement. However, the effect of the exoskeleton differed between the experiment and the model. In the experimental data, the knee-angle range appeared to decrease with the Laevo, whereas in the model the exoskeleton mainly changed the first half of the movement and had little effect in the second half. The absolute values should not be compared directly, because the experimental knee angle was calculated as a marker-based proxy, while the model value was extracted directly from the model's knee coordinate.

D. *Effects for hip and leg muscle activation*

In this section, the results for the third hypothesis, that the use of a back-support exoskeleton changes hip or leg muscle activation, are presented. Both the experimental and modelling results are shown in Figure 8.

For the gluteus medius, the experimental peak values were similar between conditions, while the average activation was higher with the Laevo. In the modelling results, gluteus medius activation remained below 10% in both conditions, although the activation during the stooping phase was higher with the exoskeleton than without the exoskeleton.

For the biceps femoris, the experimental activation pattern was more variable, with less clearly visible peaks. Without the exoskeleton, both the peak and average activation were higher than with the Laevo. In the modelling results, the activation decreased during the standing-up phase and was lower with the exoskeleton than without the exoskeleton. During the stooping phase, the modelled activation was higher with the exoskeleton.

For the rectus femoris, the experimental peak activation was lower with the Laevo than without the exoskeleton, while the average activation was higher with the Laevo. In the modelling results, rectus femoris activation was almost zero during the standing-up phase. During the stooping phase, the model showed a short activation peak.

To determine whether the observed experimental differences were statistically significant, paired-sample t-tests were performed for the participants for whom both conditions were available. The paired comparisons were based on five participants for the gluteus medius, four participants for the biceps femoris, and two participants for the rectus femoris. The results are presented in Table IV.

For the gluteus medius, neither peak nor average activation differed significantly between conditions. For the biceps femoris, peak activation did not differ significantly between conditions, but average activation was significantly lower with the Laevo. For the rectus femoris, neither peak nor average activation differed significantly between conditions.

E. *Power analysis for future experimental studies*

Because several statistical comparisons were based on a small number of valid paired participants, a power analysis was performed to estimate the sample sizes required for future

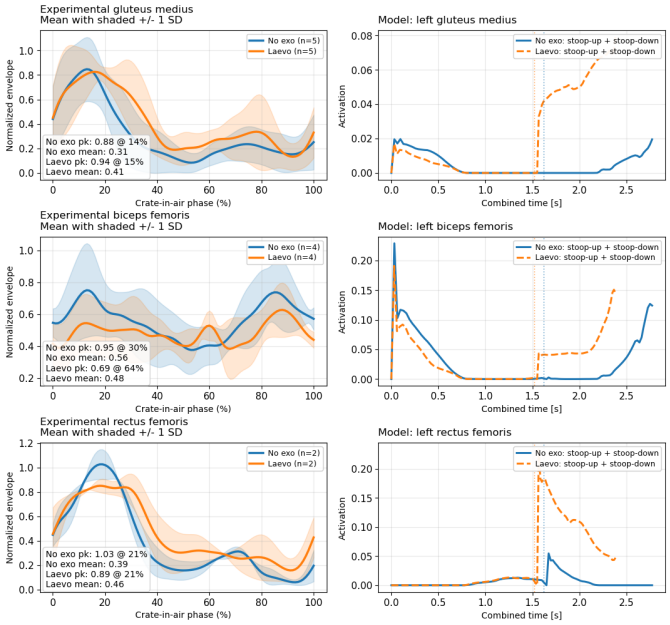

Fig. 8. Experimental and modelled activation patterns of the gluteus medius, biceps femoris, and rectus femoris with and without the Laevo. The experimental results show muscle-specific changes rather than a general increase or decrease in hip and leg activation, with the clearest effect being lower average biceps femoris activation with the Laevo. The model reproduced this lower biceps femoris activation during the standing-up phase, but differed from the experimental results in timing and magnitude, particularly because gluteus medius activation remained low and rectus femoris activation was almost absent during standing up.

TABLE IV
PAIRED-SAMPLE T-TEST RESULTS FOR NORMALIZED HIP AND LEG MUSCLE ACTIVATION IN THE 5 KG CRATE CONDITION WITH AND WITHOUT THE LAEVO. MEAN DIFFERENCES ARE CALCULATED AS LAEVO MINUS NO EXOSKELETON.

Muscle	Measure	No exo	Laevo	Diff.	t	p	d_z
G. medius	Peak	0.882	0.936	0.054	0.353	0.742	0.158
G. medius	Average	0.315	0.408	0.093	1.642	0.176	0.734
B. femoris	Peak	0.952	0.690	-0.262	-1.540	0.221	-0.770
B. femoris	Average	0.563	0.484	-0.079	-4.904	0.016	-2.452
R. femoris	Peak	1.029	0.888	-0.141	-0.773	0.581	-0.546
R. femoris	Average	0.389	0.462	0.073	1.925	0.305	1.361

studies. For a two-sided paired-sample test with $\alpha = 0.05$ and power = 0.80, the estimated required sample size was 15 paired participants for a large effect size ($d_z = 0.8$), 34 paired participants for a medium effect size ($d_z = 0.5$), and 90 paired participants for a small effect size ($d_z = 0.3$).

IV. Discussion

A. Back muscle activation

The first hypothesis stated that back muscle activation would decrease when wearing the Laevo. The experimental back muscle activation results are presented in the top plot of Figure 5, and the corresponding statistical values are shown in Table II. No significant differences were found between the Laevo and no-exoskeleton conditions for either peak or average activation. Therefore, the present results do not provide evidence for a reduction in back muscle activation during the stooping task, and the first hypothesis is not supported.

This finding is broadly consistent with previous literature, which shows mixed and phase-dependent effects of the Laevo on back muscle activation during stoop lifting. [28] investigated stoop lifting with the Laevo Flex using 5 kg and 15 kg boxes and reported overall EMG reductions of $7.3 \pm 7.8\%$ for lumbar muscles and $2.1 \pm 7.4\%$ for thoracic muscles. These reductions were modest and variable, and significant differences were only found during specific parts of the lifting cycle. Similarly, [29], a study that used an earlier Laevo version rather than the Laevo Flex, reported significant main and interaction effects of the exoskeleton on erector spinae activity, but the observed changes were small and depended on lifting style, lifting orientation, and the EMG outcome measure used. Across conditions, low-level erector spinae activity increased, whereas median and high activity levels decreased only slightly. [30] reported larger descriptive reductions in erector-spinae EMG-derived neuromuscular activation during symmetrical stooping with a 4.1 kg load, with mean activation decreasing by 51.2% and peak activation by 34.8%, but these values were not accompanied by inferential statistics and should therefore be interpreted cautiously. Finally, [31] did not find significant reductions in back muscle activation for the Laevo Flex during stooping. Taken together, these studies suggest that the effect of the Laevo on back muscle activation during stooping is variable across studies and may depend on the exoskeleton version, task, analysis window, lifting style, and outcome measure used.

Several methodological and task-related factors may explain why no significant reduction was found in the present study. First, the paired sample size was small, with only five participants having valid data in both conditions, which limited the statistical power to detect small or variable effects. Second, the effect may have depended on the specific outcome measure and analysis window. In the present study, average activation shifted slightly upward while peak activation shifted slightly downward, suggesting that a single full-movement metric may not fully capture how the exoskeleton affects muscle activation. Third, the 5 kg crate may have limited the observable difference between conditions, although the upper-body mass already contributes substantially to the mechanical demand during stooping. Therefore, the absence of a clear effect cannot be explained by the external load alone. Finally, participants were new to the Laevo and may not have fully adapted their movement strategy to use its support fully. Future studies should therefore include larger paired samples, heavier or multiple load conditions, familiarization sessions, and phase-specific analyses of muscle activation.

For the modelling results, muscle activation with the exoskeleton was generally similar to activation without the exoskeleton. This qualitatively agrees with the experimental results, where no significant difference in back muscle activation was found between conditions. The time-dependent activation profiles showed some differences between model and experiment. The short activation spike at the start of the

simulation, around $t = 0.0$, was most likely a modelling artefact related to the imposed initial conditions, such as the requirement to start from a stationary posture. The first main activation peak, around $t = 0.25$, showed reasonable agreement with the experimental activation pattern, although the model peak occurred slightly earlier. This timing difference may also be related to the imposed boundary conditions and the predictive nature of the simulation.

In the second half of the movement, the agreement between model and experiment was weaker. The experimental results showed only a small activation peak in the exoskeleton condition, whereas the model predicted clearer peaks in several muscles. This suggests that the model did not fully capture the muscle-control strategy used by participants during this phase. A possible explanation is that the effort-minimization objective encouraged the model to keep activation low until muscle force was mechanically required, resulting in sharper activation peaks than observed experimentally. Therefore, although the model captured the limited overall effect of the exoskeleton, it was less accurate in predicting the timing and shape of the activation profiles, particularly during the second half of the movement.

B. Movement changes

The second hypothesis stated that the use of the exoskeleton would change the user's motion. To study this, two outcome measures were used: the shoulder-hip distance range as a proxy for back flexion, shown in Figure 6, and the knee-angle pattern, shown in Figure 7.

For the shoulder-hip distance range, the exoskeleton decreased the range in most cases. Although the shoulder-hip distance is not a direct measure of back flexion, it can be used as a proxy in this forward-stooping task. A larger range indicates a larger difference between the most upright and most flexed posture, so the observed decrease suggests a reduction in back flexion range or a change in movement strategy when using the Laevo. This is in line with [32], who also reported smaller ranges of motion in the back when using the Laevo. However, the experimental differences as presented in Table III were not statistically significant, so this result should be interpreted as a trend rather than evidence for an effect. The strongest trend was found in the empty crate condition, where the p-value approached but did not reach the conventional significance threshold of 0.05 ($p = 0.090$). The model showed the same direction of change as the experimental trials, with a smaller shoulder-hip distance range when the exoskeleton was included. This suggests that, despite the simplifications in the exoskeleton implementation, the model captured part of the movement adaptation seen in the experimental data. The exact difference values should still be interpreted with care, since the shoulder-hip distance was not normalized to participant height or segment length and does not show where along the trunk the flexion occurred.

For the knee angle, no statistical test was performed because the full movement pattern was of interest rather than a single summary value. In the experimental results, the no-exoskeleton condition was mostly above the exoskeleton condition at the start and end of the lifting cycle, while it was below it in the middle of the cycle. This suggests that the knee angle range of motion was smaller when using the exoskeleton. However, since no statistical test was performed, this result cannot be used to confirm or reject the hypothesis. This cautious interpretation is in line with [32], who also did not find a significant effect of Laevo use on peak knee flexion, but noted a tendency towards smaller range of motion.

For the modelling results, the no-exoskeleton simulation showed a knee flexion-extension pattern that was similar in shape to the experimental results. This suggests that the model could reproduce the general knee-motion pattern without the exoskeleton. However, the exoskeleton condition differed substantially during the standing-up phase, more than was seen in the experimental results. During the stooping phase, the modelled knee angle changed only little between conditions, while a larger change would have been expected based on the experimental trend. Therefore, the model showed only partial agreement with the experimental knee-angle results.

Overall, hypothesis two was not statistically supported. The shoulder-hip distance results suggest a possible trend towards a reduced trunk flexion range when using the Laevo, with the strongest trend found in the empty crate condition. The model showed partial qualitative agreement for the shoulder-hip distance trend and for the general no-exoskeleton knee-motion pattern, but not for all exoskeleton-related knee-angle changes.

C. Hip and knee muscle activation

The third hypothesis stated that the use of the exoskeleton would change hip or leg muscle activation. The experimental results partly supported this hypothesis. The clearest finding was a statistically significant decrease in average biceps femoris activation when using the Laevo. This is in line with [29], who reported reduced biceps femoris activity when using the Laevo during lifting. Since the biceps femoris contributes to hip extension, this result suggests that the exoskeleton may have reduced the muscular demand for hip extension during the lifting task. However, the peak biceps femoris activation was not significantly different, and the comparison was based on only four paired participants. Therefore, this finding should be interpreted with caution.

For the gluteus medius and rectus femoris, no statistically significant differences were found. The peak values were similar or lower when using the Laevo, while the average values were higher. This indicates that the effect of the exoskeleton was not a general reduction in hip and leg muscle activation. Instead, the changes may have depended on the muscle and on the timing within the lifting movement. This is consistent with previous work showing that passive back-support exoskeletons can reduce activity in some muscles while increasing or not changing activity in others [29], [32].

The modelling results showed partial qualitative agreement with the experimental results. During the standing-up phase, the gluteus medius and biceps femoris showed a similar

direction of change in the model as in the experiments, with lower peak activation when the exoskeleton was included. However, the model also showed sharper initial activation peaks than the experimental data. This may be related to the model starting from zero activation, whereas the experimental EMG signals already had non-zero activation at the start of the analysed movement. The rectus femoris was almost inactive in the model during the standing-up phase, while it was active in the experimental results, suggesting that the model did not fully reproduce the experimental knee-related muscle coordination.

During the stooping phase, the model predicted higher activation with the exoskeleton for all included hip and leg muscles. Although the relative increase was large, the absolute activation values remained small. This difference may be related to the optimiser choosing a different solution path when the exoskeleton was included, especially because the timing of the motion differed between model conditions. Therefore, the stooping-phase muscle activation results should be interpreted as a modelling outcome rather than as direct validation against the experimental data.

Overall, hypothesis three was only partly supported. The experimental results showed a statistically significant decrease in average biceps femoris activation, but the other hip and leg muscle differences were not statistically significant. The model showed partial qualitative agreement during the standing-up phase, especially for the gluteus medius and biceps femoris, but not for all muscles or movement phases. Therefore, the model comparison should be interpreted as preliminary qualitative agreement rather than validation.

V. Limitations and future work

This thesis should be interpreted as a proof of concept for combining experimental measurements with predictive simulations of passive back-support exoskeleton use. Several limitations affected both the experimental and modelling parts of the study. These limitations do not invalidate the main findings, but they restrict the extent to which the results can be generalised and quantitatively interpreted.

A. Experimental limitations

The experimental measurements were performed in a controlled laboratory setting. This allowed the lifting task and measurement setup to be standardised, but it also means that the results may not fully represent real occupational use of the Laevo. In practice, lifting and bending tasks involve more variation in posture, movement speed, load, fatigue, and user behaviour than was included in this study. In addition, only short-term effects were evaluated, so possible long-term adaptations in movement strategy were not assessed. The use of a 5 kg crate and a standardised stooping movement may therefore not have captured the conditions in which the Laevo support is most strongly engaged. As a result, the experimental findings should be interpreted as task-specific trends rather than as general effects of Laevo use. Future work should include more varied lifting and bending tasks, different external loads, longer use durations, and measurements in occupational or semi-field settings.

A second limitation was the limited amount of complete participant data. Although nine participants were measured, not all participants had valid data for all muscles, markers, trials, and conditions. Data loss was mainly caused by practical issues such as loose electrodes, loose markers, and contact artefacts between the exoskeleton and the EMG electrodes. This reduced the number of paired comparisons, decreased statistical power, and increased the uncertainty around the estimated effects. Therefore, the non-significant results should not be interpreted as strong evidence that the Laevo had no effect, especially since the power analysis indicated that at least 90 participants would be required to reliably detect a small effect. Larger paired samples, together with improved electrode and marker placement, would therefore be needed to detect smaller effects more reliably.

The EMG results should also be interpreted as relative trends rather than absolute activation levels. The signals were not normalised to maximum voluntary contractions, which means that activation magnitudes cannot be directly compared between muscles or participants. This does not prevent within-participant comparison between the no-exoskeleton and Laevo conditions, but it limits conclusions about absolute muscle activation. Future studies should include maximum voluntary contractions or another standardised reference contraction to improve between-participant comparison and model validation.

B. Predictive modelling limitations

Several simplifications were required to obtain converging predictive simulations. The model was restricted to a sagittal-plane task and the feet were welded to the ground. These assumptions were consistent with the simplified experimental stooping task, which supports comparison between the experimental and modelling results. However, the same simplification also means that both parts of the study excluded variations that may occur during real exoskeleton use, such as asymmetrical movement, balance corrections, foot repositioning, and frontal- or transverse-plane compensations. The results should therefore be interpreted as specific to a standardised sagittal-plane stooping task. Future work should extend the framework to less constrained and more three-dimensional tasks, including asymmetric lifting and movements with more natural foot-ground interaction.

No external crate load was included in the predictive simulations. Therefore, the model did not directly reproduce the experimental 5 kg lifting condition. This may have reduced the predicted muscle demands and may also have affected the predicted benefit of the Laevo, because the support torque may become more relevant when external load demands are higher. The current simulations should therefore be interpreted as unloaded stooping and standing-up simulations with and without Laevo support. Future simulations should include external hand or crate loads to allow a more direct comparison with the experimental lifting trials.

The muscle-driven model was also simplified. Only a subset of muscles was included to improve convergence, and the hip/leg and back muscle simulations were not solved as one fully integrated muscle-driven problem. This split was considered acceptable for this proof-of-concept study because the selected muscle groups mainly actuated different model coordinates, but it remains a simplification of full-body coordination. However, it still prevented the model from capturing possible interactions in full-body force-sharing and compensatory strategies between the lower limbs and trunk. For the hip and leg muscles, the main agonists were included and reserve actuator torques remained below the accepted threshold. For the back, the included muscle set was more limited and reserve actuator use remained higher. Therefore, the predicted back-muscle activation magnitudes should be interpreted cautiously. The timing and qualitative activation patterns may be more reliable than the absolute magnitudes, but this remains uncertain because the results also depend on muscle force-sharing, reserve actuator use, and the selected objective function. Future work should gradually increase the number of included trunk and lower-limb muscles and move towards a fully integrated muscle-driven model with lower reserve actuator contributions.

The muscle model settings were simplified by using `DeGrooteFregly2016Muscle` components while ignoring tendon compliance and passive fibre forces. These choices improved convergence, but removed passive tissue contributions that may be relevant during stooping and standing up. This may have affected the predicted activation magnitudes and could have contributed to activation peaks that were not clearly observed in the experimental EMG. Future work should investigate the effect of adding passive fibre forces and tendon compliance once the model can solve reliably.

The predictive simulations also depended on the selected objective function and solver settings. The objective included minimising effort and time, but human lifting strategies may also prioritise stability, comfort, smoothness, or task consistency. In addition, the model was generic rather than participant-specific, so individual differences in body dimensions, muscle geometry, and strength were not represented. The simulations were solved with relatively loose convergence settings and limited mesh density, which may have affected small timing differences, short activation peaks, or subtle differences between conditions. These factors are unlikely to invalidate the qualitative comparison between the no-exoskeleton and Laevo simulations, but they limit detailed quantitative interpretation. Future work should therefore include sensitivity analyses for objective-function terms, initial guesses, initial joint angles, initial muscle activations, mesh density, convergence settings, and participant-specific model parameters.

Finally, the Laevo was represented as an angle-dependent hip torque. This allowed the experimentally derived angle-torque behaviour to be implemented in OpenSim Moco, but it simplified the real exoskeleton-user interaction. In reality, the Laevo applies forces through contact points at the chest, pelvis, and thighs. Representing this as a pure hip torque ignores the distribution of these forces over the body and limits quantitative interpretation of posture, muscle activation, and joint loading. Future work should model the Laevo using distributed interaction forces at the relevant body contact points.

VI. Conclusion

This thesis aimed to develop and evaluate a proof-of-concept OpenSim Moco framework for predictive modelling of a passive back-support exoskeleton during stooping. The first hypothesis stated that back muscle activation would be reduced by the Laevo. However, the experimental results did not show a significant reduction in erector spinae activation. The second hypothesis stated that the Laevo would change the motion of the user during stooping. The shoulder-hip distance results suggested a trend towards a smaller motion range when using the Laevo, but this was not statistically significant. A similar trend was found in the model results. The third hypothesis concerned possible changes in hip or leg muscle activation. Clear statistical evidence for a general change was not found, although average biceps femoris activation decreased significantly and some experimental trends were partly reflected in the model results.

Overall, the framework could be used to generate predictive simulations with and without exoskeleton support. However, the current results should be interpreted as a preliminary proof-of-concept rather than as quantitative validation of the model. The main limitations of this study were the small number of valid paired participants, the use of a generic non-subject-specific model, the simplified representation of the Laevo as a hip torque rather than as distributed interaction forces, and the remaining convergence and reserve-actuator limitations in the predictive simulations.

The main contribution of this thesis is therefore the development of a reproducible modelling workflow and an initial assessment of how such a model can be compared with experimental EMG and motion-capture trends. Future research should focus on larger experimental datasets, improved subject-specific modelling, and a more detailed representation of the physical interaction between the user and the exoskeleton in the model.

REFERENCES

[1] World Health Organisation, "Musculoskeletal health," https://www.who.int/news-room/fact-sheets/detail/musculoskeletal-conditions, Jul. 2022.

[2] ——, "Low back pain," https://www.who.int/news-room/fact-sheets/detail/low-back-pain, Jun. 2023.

[3] National Institute for Occupational Safety and Health (NIOSH), "Step 1: Identify Risk Factors," https://www.cdc.gov/niosh/ergonomics/ergo-programs/risk-factors.html, Jan. 2024.

[4] OSHA, "Musculoskeletal disorders," https://osha.europa.eu/en/themes/musculoskeletal-disorders.

[5] Health and Safety Executive, "Construction physical ill health risks: Manual handling," https://www.hse.gov.uk/construction/healthrisks/physical-ill-health-risks/manual-handling.htm.

[6] U.S. Government Accountability Office, "Workplace Safety and Health: OSHA Should Take Steps to Better Identify and Address Ergonomic Hazards at Warehouses and Delivery Companies," https://www.gao.gov/products/gao-24-106413, Sep. 2024.

[7] A. Ali, V. Fontanari, W. Schmoelz, and S. K. Agrawal, "Systematic Review of Back-Support Exoskeletons and Soft Robotic Suits," *Frontiers in Bioengineering and Biotechnology*, vol. 9, p. 765257, Nov. 2021.

[8] J. W. Ramsay, C. L. Hancock, M. P. O'Donovan, and T. N. Brown, "Soldier-relevant body borne loads increase knee joint contact force during a run-to-stop maneuver," *Journal of Biomechanics*, vol. 49, no. 16, pp. 3868–3874, Dec. 2016.

[9] A. C. C. De Sousa and J. M. Font-Llagunes, "Predictive Framework for Electrical Stimulation Cycling in Spinal Cord Injury," *IFAC-PapersOnLine*, vol. 58, no. 24, pp. 332–337, 2024.

[10] E. Mathieu, S. Crémoux, D. Duvivier, D. Amarantini, and P. Pudlo, "Biomechanical modeling for the estimation of muscle forces: Toward a common language in biomechanics, medical engineering, and neurosciences," *Journal of NeuroEngineering and Rehabilitation*, vol. 20, no. 1, p. 130, Sep. 2023.

[11] A. Golabchi, A. Chao, and M. Tavakoli, "A Systematic Review of Industrial Exoskeletons for Injury Prevention: Efficacy Evaluation Metrics, Target Tasks, and Supported Body Postures," *Sensors*, vol. 22, no. 7, p. 2714, Apr. 2022.

[12] A. S. Koopman, I. Kingma, G. S. Faber, M. P. De Looze, and J. H. Van Dieën, "Effects of a passive exoskeleton on the mechanical loading of the low back in static holding tasks," *Journal of Biomechanics*, vol. 83, pp. 97–103, Jan. 2019.

[13] T. Luger, M. Bär, R. Seibt, M. A. Rieger, and B. Steinhilber, "Using a Back Exoskeleton During Industrial and Functional Tasks—Effects on Muscle Activity, Posture, Performance, Usability, and Wearer Discomfort in a Laboratory Trial," *Human Factors: The Journal of the Human Factors and Ergonomics Society*, vol. 65, no. 1, pp. 5–21, Feb. 2023.

[14] S. Kranenborg, C. Greve, M. Reneman, and C. Roossien, "Side-effects and adverse events of a shoulder- and back-support exoskeleton in workers: A systematic review," *Applied Ergonomics*, vol. 111, p. 104042, Sep. 2023.

[15] A. Seth, J. L. Hicks, T. K. Uchida, A. Habib, C. L. Dembia, J. J. Dunne, C. F. Ong, M. S. DeMers, A. Rajagopal, M. Millard, S. R. Hamner, E. M. Arnold, J. R. Yong, S. K. Lakshmikanth, M. A. Sherman, J. P. Ku, and S. L. Delp, "OpenSim: Simulating musculoskeletal dynamics and neuromuscular control to study human and animal movement," *PLOS Computational Biology*, vol. 14, no. 7, p. e1006223, Jul. 2018.

[16] M. Damsgaard, J. Rasmussen, S. T. Christensen, E. Surma, and M. De Zee, "Analysis of musculoskeletal systems in the AnyBody Modeling System," *Simulation Modelling Practice and Theory*, vol. 14, no. 8, pp. 1100–1111, Nov. 2006.

[17] S. L. Delp, F. C. Anderson, A. S. Arnold, P. Loan, A. Habib, C. T. John, E. Guendelman, and D. G. Thelen, "OpenSim: Open-Source Software to Create and Analyze Dynamic Simulations of Movement," *IEEE Transactions on Biomedical Engineering*, vol. 54, no. 11, pp. 1940–1950, Nov. 2007.

[18] C. L. Dembia, N. A. Bianco, A. Falisse, J. L. Hicks, and S. L. Delp, "OpenSim Moco: Musculoskeletal optimal control," *PLOS Computational Biology*, vol. 16, no. 12, p. e1008493, Dec. 2020.

[19] F. De Groote and A. Falisse, "Perspective on musculoskeletal modelling and predictive simulations of human movement to assess the neuromechanics of gait," *Proceedings of the Royal Society B: Biological Sciences*, vol. 288, no. 1946, p. 20202432, Mar. 2021.

[20] S. Amandels, H. O. H. Eyndt, L. Daenen, and V. Hermans, "Introduction and Testing of a Passive Exoskeleton in an Industrial Working Environment," in *Proceedings of the 20th Congress of the International Ergonomics Association (IEA 2018)*, S. Bagnara, R. Tartaglia, S. Albolino, T. Alexander, and Y. Fujita, Eds. Cham: Springer International Publishing, 2019, vol. 820, pp. 387–392.

[21] S. M. McGill, "Electromyographic activity of the abdominal and low back musculature during the generation of isometric and dynamic axial trunk torque: Implications for lumbar mechanics," *Journal of Orthopaedic Research*, vol. 9, no. 1, pp. 91–103, Jan. 1991.

[22] Peter Konrad, *The ABC of EMG: A Practical Introduction to Kinesiological Electromyography*, 1st ed. Scottsdale, Arizona, USA: Noraxon U.S.A., Inc., 2006.

[23] H.J. Hermens, B Freriks, and R. Merletti, "SENIAM," http://seniam.org, Enchede.

[24] N. Riahi, N. Jasimi Zindashti, A. Golabchi, M. Tavakoli, and H. Rouhani, "Musculoskeletal Modeling of a Hinge-Type Back-Support Exoskeleton: A Simplified Approach for Practical Assessment," *Annals of Biomedical Engineering*, vol. 54, no. 1, pp. 195–210, Jan. 2026.

[25] J. R. Potvin, R. W. Norman, and S. M. McGill, "Mechanically corrected EMG for the continuous estimation of erector spinae muscle loading during repetitive lifting," *European Journal of Applied Physiology and Occupational Physiology*, vol. 74, no. 1-2, pp. 119–132, Aug. 1996.

[26] A. G. Bruno, M. L. Bouxsein, and D. E. Anderson, "Development and Validation of a Musculoskeletal Model of the Fully Articulated Thoracolumbar Spine and Rib Cage," *Journal of Biomechanical Engineering*, vol. 137, no. 8, p. 081003, Aug. 2015.

[27] Delft High Performance Computing Centre (DHPC), "DelftBlue Supercomputer (Phase 2)," https://www.tudelft.nl/dhpc/ark:/44463/DelftBluePhase2, 2024.

[28] A. Moya-Esteban, G. Durandau, H. Van Der Kooij, and M. Sartori, "Real-time lumbosacral joint loading estimation in exoskeleton-assisted lifting conditions via electromyography-driven musculoskeletal models," *Journal of Biomechanics*, vol. 157, p. 111727, Aug. 2023.

[29] T. Luger, M. Bär, R. Seibt, P. Rimmele, M. A. Rieger, and B. Steinhilber, "A passive back exoskeleton supporting symmetric and asymmetric lifting in stoop and squat posture reduces trunk and hip extensor muscle activity and adjusts body posture – A laboratory study," *Applied Ergonomics*, vol. 97, p. 103530, Nov. 2021.

[30] Y. Zhou, J. Seo, Y. Gong, K. H. Heung, M. Khan, and T. Lei, "Biomechanical assessment of a passive back exoskeleton using vision-based motion capture and virtual modeling," *Automation in Construction*, vol. 172, p. 106035, Apr. 2025.

[31] M. I. Mohamed Refai, A. Moya-Esteban, L. Van Zijl, H. Van Der Kooij, and M. Sartori, "Benchmarking commercially available soft and rigid passive back exoskeletons for an industrial workplace," *Wearable Technologies*, vol. 5, p. e6, 2024.

[32] S. J. Baltrusch, J. H. Van Dieën, S. M. Bruijn, A. S. Koopman, C. A. M. Van Bennekom, and H. Houdijk, "The effect of a passive trunk exoskeleton on metabolic costs during lifting and walking," *Ergonomics*, vol. 62, no. 7, pp. 903–916, Jul. 2019.

APPENDIX A
EXTRACTING THE PRBS SIGNAL FROM THE MOTION-CAPTURE DATA AND ALIGNING IT WITH THE EMG DATA

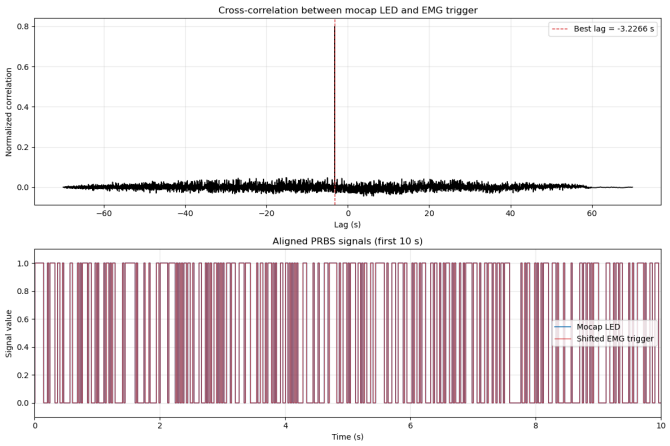

Fig. 9. Example result of the cross-correlation-based synchronisation procedure for one trial. The top plot shows one clear peak in the normalized cross-correlation, indicating the estimated delay between the EMG and motion-capture PRBS signals. The bottom plot shows that applying this delay aligns the two trigger signals, allowing the EMG data to be analysed on the motion-capture timeline.

To synchronise the motion-capture and EMG recordings, the pseudo-random binary sequence (PRBS) was reconstructed directly from the motion-capture data. During the experiment, the PRBS was generated by an infrared LED that switched on and off according to the trigger sequence. In the exported Qualisys `.mat` files, this LED did not appear as a labelled marker, but as one or more trajectories in `Trajectories.Unidentified`. For each trial, the unidentified marker data were converted to an array with shape marker $\times$ frame $\times$ coordinate from `Trajectories.Unidentified.Data`. Candidate LED markers were then selected based on their location: any unidentified trajectory for which the second coordinate, y, was smaller than -500 mm in at least one frame was retained as a possible LED marker. This spatial criterion was chosen because the LED was located behind the participant, in a region that the participant could not enter during the task. As an additional validation step, the centroids of the selected candidate trajectories were compared. In the exploratory script, a warning was issued if the maximum distance between candidate centroids exceeded 5 mm, to verify that the selected trajectories originated from the same physical location.

After this spatial preselection, the PRBS itself was reconstructed from the Qualisys unidentified-marker `Type` information rather than from the marker coordinates. This was necessary because the coordinate data could be affected by gap filling, which would smooth over brief LED on/off transitions and therefore distort the binary trigger pattern. For each candidate trajectory, the corresponding row in `Trajectories.Unidentified.Type` was extracted. A single binary motion-capture PRBS signal was then formed frame by frame as

$$u_{\mathrm{mocap}}(k) = \begin{cases} 1, & \text{if at least one candidate LED trajectory} \\ & \text{had Type} = 1 \text{ in frame } k, \\ 0, & \text{otherwise.} \end{cases} \tag{2}$$

Thus, the final motion-capture PRBS was the logical OR across all selected candidate LED trajectories. The motion-capture time vector was defined from the frame numbers and the trial frame rate as

$$t_{\mathrm{mocap}}(k) = \frac{k}{f_s}, \tag{3}$$

where f_s is `trial_data.FrameRate`.

The EMG recording already contained a binary trigger channel, `trigger_binary`, and its associated time vector, `time_s`. To align the motion-capture-derived PRBS with the EMG trigger, both binary signals were first restricted to finite samples and then resampled onto a common time grid. The motion-capture and EMG sample intervals were computed as the median difference between consecutive timestamps, and the common time step was chosen as the smaller of the two:

$$\Delta t_{\mathrm{common}} = \min(\Delta t_{\mathrm{mocap}}, \Delta t_{\mathrm{EMG}}). \tag{4}$$

The common time vector ran from 0 s to the end of the longer recording. Both binary signals were mapped onto this grid using zero-order hold sampling, meaning that each common-grid sample inherited the most recent available source value.

Next, both resampled binary signals were mean-centred and their full cross-correlation was computed. The correlation was normalised by the product of the Euclidean norms of the two centred signals, yielding a normalised cross-correlation sequence. The lag corresponding to the maximum value of this sequence was taken as the synchronisation delay between EMG and motion capture. An example of this cross-correlation procedure is shown in Figure 9, where the cross-correlation contains one clear peak and the resulting PRBS signals are aligned after applying the estimated delay. In the implementation, this lag was stored both in samples and in seconds. Finally, the EMG signal was shifted by this estimated delay so that the EMG data could be expressed on the motion-capture timeline for subsequent analysis of muscle activity and movement events.

APPENDIX B
EMG PLACEMENT DETAILS

This appendix gives an overview of the EMG channel configuration and electrode placement used during the experimental measurements. The EMG setup consisted of eight bipolar surface EMG channels and one ground electrode. The measured muscles were selected to include the main back muscles of interest, as well as abdominal, hip, and leg muscles that could be affected by the use of the Laevo. Because only eight EMG channels were available, most muscles were measured on the left side only. The erector spinae longissimus was measured bilaterally, because this muscle was the main muscle used to evaluate the effect of the exoskeleton on back muscle activation.

TABLE V
EMG CHANNELS AND CORRESPONDING MEASURED MUSCLES.

Channel	Muscle	Side
1	Erector spinae longissimus	Left
2	Erector spinae iliocostalis	Left
3	External oblique	Left
4	Rectus abdominis	Left
5	Gluteus medius	Left
6	Biceps femoris	Left
7	Rectus femoris	Left
8	Erector spinae longissimus	Right

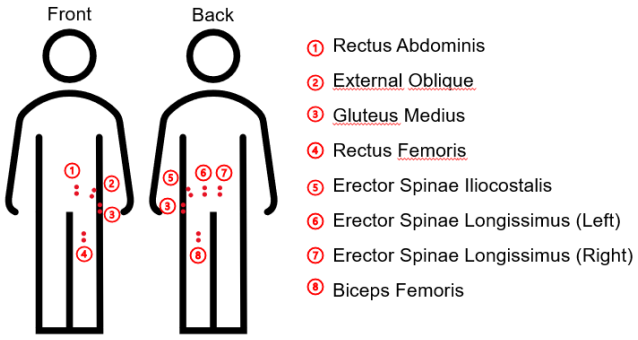

Fig. 10. Overview of locations of the EMG electrode placement. Please note the numbering is different from the channels listed in the table.

The electrode locations were chosen based on anatomical landmark descriptions from the used placement guides. The external oblique and rectus abdominis placements were based on [22], while the remaining placements were based on SENIAM [23]. For all muscles, the electrode pair was placed approximately parallel to the muscle fibre direction. The ground electrode was placed on the neck. A graphic overview of the muscle electrode placement can be found in Figure 10.

The erector spinae longissimus electrodes were placed over the longissimus muscle belly, approximately parallel to the spine. This placement was used on both the left and right side. The erector spinae iliocostalis electrodes were placed on the left side, lateral to the longissimus placement, over the iliocostalis muscle belly.

The external oblique electrodes were placed on the left lateral abdominal wall, following the direction of the external oblique fibres. The rectus abdominis electrodes were placed on the left side over the rectus abdominis muscle belly, next to the midline.

The gluteus medius electrodes were placed on the left side between the iliac crest and the greater trochanter. The biceps femoris electrodes were placed on the posterior side of the left thigh, between the ischial tuberosity and the lateral side of the knee. The rectus femoris electrodes were placed on the anterior side of the left thigh, between the anterior superior iliac spine and the patella.

Some practical deviations from an ideal standardized EMG protocol were present. No specific skin preparation was performed before electrode placement, and the inter-electrode distance was not measured explicitly. Therefore, the electrode locations should be interpreted as anatomically guided surface EMG placements rather than strictly standardized SENIAM placements. The electrode and cable locations were also selected with the exoskeleton in mind. The Laevo was worn over the electrodes and markers, so the electrodes were placed such that direct contact with the main exoskeleton pads and frame was avoided as much as possible. During donning of the Laevo, the cables were routed with enough slack to reduce pulling on the electrodes during the stooping motion.

Despite these precautions, cable and electrode problems occurred during some trials. In some cases, cables were pulled loose during the movement or while donning the exoskeleton. When this happened, the electrode connection was restored and the trial was repeated. If the problem occurred repeatedly, the cable was given more slack where possible. This was especially relevant for the abdominal and hip-region electrodes, because these cables passed close to the hip padding of the Laevo and could become trapped between the exoskeleton and the body. If a usable recording could not be obtained after repeated attempts, the corresponding trial was skipped to avoid excessive testing time.

Another recurring problem was mechanical contact between the exoskeleton and the electrodes. This could create large non-physiological spikes in the EMG signal. These artefacts depended on the participant-specific fit of the exoskeleton and on the relative position of the electrodes with respect to the exoskeleton frame and padding. Because these spikes could not be removed reliably without risking distortion of the physiological EMG signal, trials with clear contact artefacts were excluded from the analysis.

APPENDIX C
MARKER PLACEMENT

This appendix provides a visual overview of the infrared marker placement used during the motion-capture measurements. The figure is included to support interpretation of the experimental setup and to indicate the approximate anatomical locations from which the motion-capture data were obtained.

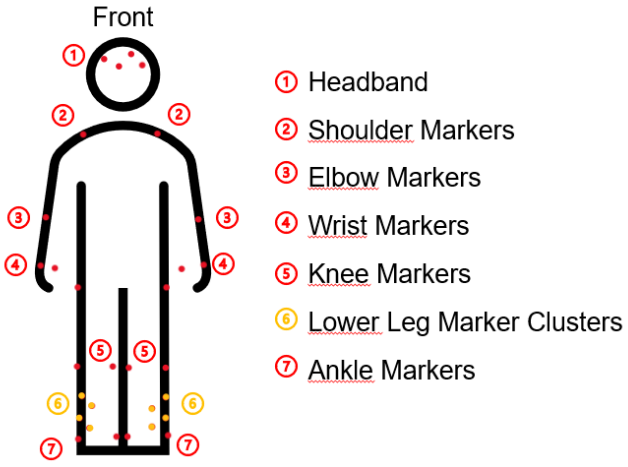

Fig. 11. Overview of the approximate placement of the infrared markers used during the motion-capture measurements. The markers were placed on anatomical landmarks and body segments to track the lifting movement during the experimental trials.

APPENDIX D
INSTRUCTIONS TO FIT THE LAEVO

This appendix shows the fitting instructions for the Laevo FLEX. The poster summarises the steps used to position and adjust the device before use, supporting consistent fitting across participants and experimental conditions.

APPENDIX E
PROCESSING WORKFLOW FOR HIP–SHOULDER DISTANCE ANALYSIS

This appendix describes the processing steps used to derive the hip-shoulder distance results used for hypothesis 2. The goal of this analysis was to quantify changes in upper-body posture during lifting by using the distance between the right hip and right shoulder markers as a proxy measure. The analysis was performed separately for the empty-crate and 5 kg crate stoop-lifting conditions, and the no-exoskeleton condition was compared with the Laevo condition.

A. Input data and trial selection

The analysis started from the cached trial metadata file `emg_mocap_lift_metadata.json`. This file already contained the relevant trial information and the cached crate-in-air intervals in seconds. Therefore, the EMG motion capture synchronization and the lift timing detection were not recomputed in this script. Instead, the previously determined lift intervals were loaded and used directly. This was done to avoid long running times and because the lift interval detection had already been finalized.

For each selected motion-capture trial, the corresponding MATLAB file was loaded. The script identified the named marker labels in the file and extracted the three-dimensional marker trajectories needed for the analysis. For the main hip-shoulder distance metric, the required markers were the right hip marker and the right shoulder marker. These marker trajectories were stored as time-dependent three-dimensional coordinates.

The comparison was made between the two experimental series:

- `x`: no exoskeleton;
- `Lae`: Laevo exoskeleton.

The analysis was performed for the stoop-lifting trials with an empty crate and with a 5 kg crate. Trials were selected based on their condition labels as previously set for the cached file, for example `crate stoop` and `crate 5 stoop`. The selected trials were stored per participant and per condition, so that paired comparisons between the no-exoskeleton and Laevo conditions could be made later.

B. Lift interval masking

For each trial, the cached crate-in-air intervals were used to determine which motion-capture frames belonged to a lift. The lift intervals were stored in seconds. These time intervals were converted to frame indices using the motion-capture time vector. A boolean mask was then created to indicate whether each frame occurred during a lifting interval. This mask was used to distinguish frames during lifting from the rest of the trial.

C. Marker validity check

Before a trial was used for the hip-shoulder distance analysis, marker validity was checked. A frame was considered valid only when all required marker coordinates were finite. For the hip-shoulder distance metric, this meant that both the right hip and right shoulder marker coordinates had to be valid in the same frame.

Two validity fractions were computed for each trial:

- the fraction of valid frames over the full trial;
- the fraction of valid frames during the lift intervals only.

For the main distance analysis, a trial was included only when the marker validity during the lift intervals was at least 90%. This ensured that the calculated lift-level distance ranges were based on sufficiently complete marker trajectories during the relevant part of the movement.

D. Calculation of hip-shoulder distance

The marker positions and projected distance used for this calculation are illustrated in Figure 12.

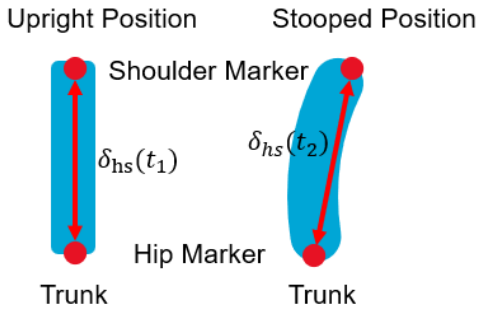

Fig. 12. Graphic view of the distance calculated for the hip-shoulder distance. The image shows the trunk in an upright and in a flexed position, as well as the hip and shoulder markers and the distances that were calculated.

The hip-shoulder distance was calculated frame by frame. Only the y- and z-coordinates of the marker trajectories were used, since the distance was projected into the sagittal plane. For each frame, the vector from the right hip marker to the right shoulder marker was calculated in the y-z plane, where the subscripts s and h denote the shoulder and hip markers, respectively:

$$\begin{aligned} \Delta \mathbf{r}_{yz}(t) &= \begin{bmatrix} y_s(t) - y_h(t) \\ z_s(t) - z_h(t) \end{bmatrix}, \\ d_{hs}(t) &= \left\| \Delta \mathbf{r}_{yz}(t) \right\|_2 \\ &= \sqrt{(y_s(t) - y_h(t))^2 + (z_s(t) - z_h(t))^2}, \end{aligned} \tag{5}$$

The resulting distance trace was expressed in millimetres and stored together with the corresponding time vector. This trace represented the time-varying distance between the right hip and right shoulder marker in the sagittal-plane-related y-z projection.

E. Visualization of raw distance traces

For visual inspection, the full hip-shoulder distance trace was plotted for each selected participant and condition. The no-exoskeleton and Laevo trials were plotted separately. The cached crate-in-air intervals were shown as grey shaded regions in the plots. These plots were used to inspect the raw

distance traces and to verify whether the selected lift intervals corresponded to the intended lifting movements. The grey shaded intervals were not used as an additional processing step, they only indicated the parts of the trace over which the lift-level metrics were calculated.

F. Reduction to lift-level range values

Each individual lift was reduced to one summary value. For every cached crate-in-air interval, the part of the hip–shoulder distance trace within that interval was extracted. This lift-specific trace was then time-normalized to 101 points, corresponding to 0–100% of the lift. Linear interpolation was used for the normalization.

After normalization, the range of the hip-shoulder distance during the lift was calculated as:

$$\mathrm{range}_d = \max(d_{\mathrm{hip-shoulder}}) - \min(d_{\mathrm{hip-shoulder}}).$$

Thus, each lift received one distance-change value in millimetres. This value described how much the right hip-shoulder distance changed during that lift, independent of the absolute starting distance.

G. Participant-level averaging

When a participant had multiple valid lifts within a trial, the lift-level ranges were averaged. This resulted in one participant-level mean hip-shoulder distance range for each participant, condition, and series. In other words, for each included participant, the analysis produced:

$$\overline{\mathrm{range}}_{d,\mathrm{x}}$$

for the no-exoskeleton condition and

$$\overline{\mathrm{range}}_{d,\mathrm{Lae}}$$

for the Laevo condition.

Only participants for whom both the no-exoskeleton and Laevo values were available were included in the paired comparison. The statistical analysis was therefore performed on participant-average lift ranges, not on individual frames or individual lifts.

H. Comparison between no-exoskeleton and Laevo conditions

The same procedure was applied separately to the empty-crate and 5 kg crate stoop-lifting conditions. For each load condition, the participant-level mean hip-shoulder distance range was compared between the no-exoskeleton and Laevo series.

For each load condition, a paired t-test was performed on the participant-level values. The paired comparison used the difference:

$$\Delta\mathrm{range}_d = \overline{\mathrm{range}}_{d,\mathrm{Lae}} - \overline{\mathrm{range}}_{d,\mathrm{x}}.$$

The script also calculated the mean difference, the 95% confidence interval of the mean difference, Cohen's d_z, and a priori sample-size estimates for selected target effect sizes. Because the statistical test used participant-average values, each participant contributed only one paired value per condition.

I. Comparison with model results

The experimental hip-shoulder distance results were also compared with corresponding model-based results when OpenSim model solutions were available. For the model, the latest matching `.sto` solution files were loaded. The model-based distance was calculated between the pelvis and the right humerus body. Unlike the experimental metric, which was calculated in the motion-capture (y)–(z) plane, the model distance was calculated in the model (x)–(y) plane. This plane corresponded to the sagittal plane and was referred to in the script as the front–up plane. For compactness, (h) denotes the right humerus body and (p) denotes the pelvis body:

$$d_{\mathrm{model}}(t) = \sqrt{\left(x_h(t) - x_p(t)\right)^2 + \left(y_h(t) - y_p(t)\right)^2}. \tag{6}$$

The model trace was summarized using the same range metric:

$$\mathrm{range}_{d,\mathrm{model}} = \max(d_{\mathrm{model}}) - \min(d_{\mathrm{model}}).$$

The model distance ranges were originally obtained in metres and were converted to millimetres before plotting them together with the experimental participant-level results. The final comparison plot therefore contained no-exoskeleton and Laevo values for the empty-crate condition, the 5 kg crate condition, and the model results.

It should be noted that the experimental and model metrics are conceptually similar but not geometrically identical. The experimental metric used the right hip-to-right shoulder marker distance in the y-z plane, whereas the model metric used the pelvis-to-right humerus distance in the x-y plane. Therefore, the comparison between experiment and model should be interpreted as a comparison of similar posture-related distance changes, not as a one-to-one validation of the same anatomical measurement.

APPENDIX F
PROCESSING WORKFLOW FOR KNEE-ANGLE PROXY ANALYSIS

This appendix describes the processing steps used to derive the knee-angle proxy results from the experiments. The goal of this analysis was to quantify changes in knee flexion during lifting and to compare the no-exoskeleton and Laevo conditions. The workflow followed the same general structure as the hip-shoulder distance analysis, but used a different marker set and a less strict per-lift validity procedure.

A. Input data and trial selection

The knee-angle analysis also started from the cached trial metadata file `emg_mocap_lift_metadata.json`. This file contained the selected trial information and the cached crate-in-air intervals in seconds. The EMG-motion capture synchronization and lift timing were therefore not recomputed in this script.

For each selected trial, the corresponding motion-capture MATLAB file was loaded. The marker labels were identified, and the three-dimensional marker trajectories required for the knee-angle proxy were extracted. The knee-angle proxy was calculated from three markers:

- hip marker;
- knee marker;
- ankle marker.

The same experimental series were compared as in the hip-shoulder distance analysis:

- `x`: no exoskeleton;
- `Lae`: Laevo exoskeleton.

The analysis was performed for the stoop-lifting trials, including the empty-crate and 5 kg crate conditions. Trials were selected using their condition labels and stored per participant, condition, and series so that participant-level comparisons could be made.

B. Lift interval definition

The cached crate-in-air intervals were used to define the lifting phases. For each trial, the lift intervals were converted from seconds to frame indices using the motion-capture time vector. These intervals determined which parts of the knee-angle trace were used for lift-level processing and normalization.

C. Knee marker validity and per-lift inclusion

For the knee-angle analysis, marker validity was evaluated at the lift level. A frame was considered valid when all required marker coordinates were finite for the hip, knee, and ankle markers. Because the knee-angle calculation requires all three markers in the same frame, a frame was excluded from the knee-angle calculation if one or more of these marker coordinates were missing or non-finite.

A lift was included only if at least 80% of the frames within that lift interval were valid. This differs from the hip-shoulder distance analysis, where trial inclusion was based on the overall validity during all lift intervals. For the knee-angle analysis, a trial was kept if it contained at least one valid lift. This made it possible to include trials where some lifts had sufficient marker visibility, even if other lifts in the same trial did not.

D. Calculation of knee-angle proxy

The marker positions, segment vectors and angles used for the knee-angle proxy calculation are illustrated schematically in Figure 13. The vector $\mathbf{v}_{\mathrm{thigh}}$ was defined from the knee marker to the hip marker, while $\mathbf{v}_{\mathrm{shank}}$ was defined from the knee marker to the ankle marker. In the schematic, α represents the included angle between these two vectors. The knee-angle proxy is indicated by β, which was defined as the deviation from a fully extended knee posture.

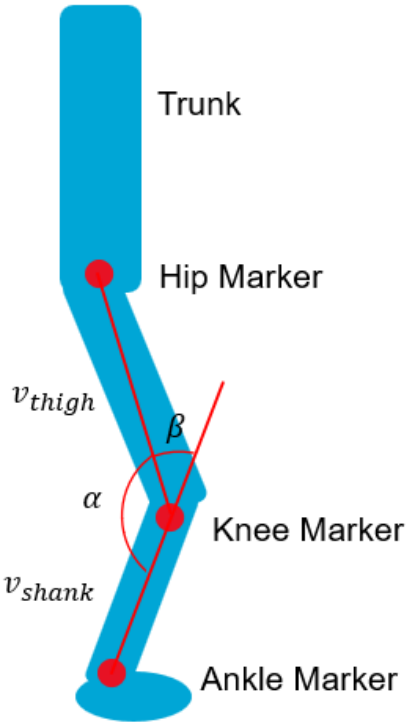

Fig. 13. Schematic illustration of the knee-angle proxy calculation. The hip, knee and ankle markers were projected onto the y-z plane. The vectors $\mathbf{v}_{\mathrm{thigh}}$ and $\mathbf{v}_{\mathrm{shank}}$ represent the thigh and shank segments, respectively. The included angle α was calculated using the dot product, and the flexion-style knee-angle proxy β was defined as $180^\circ - \alpha$.

The knee-angle proxy was calculated in the y-z plane. For each valid frame, the marker coordinates were first projected onto this plane. Two vectors were then constructed: one from the knee marker to the hip marker, representing the thigh segment, and one from the knee marker to the ankle marker, representing the shank segment:

$$\mathbf{v}_{\mathrm{thigh}}(t) = \begin{bmatrix} y_{\mathrm{hip}}(t) - y_{\mathrm{knee}}(t) \\ z_{\mathrm{hip}}(t) - z_{\mathrm{knee}}(t) \end{bmatrix},$$

$$\mathbf{v}_{\mathrm{shank}}(t) = \begin{bmatrix} y_{\mathrm{ankle}}(t) - y_{\mathrm{knee}}(t) \\ z_{\mathrm{ankle}}(t) - z_{\mathrm{knee}}(t) \end{bmatrix}.$$

The included angle between the thigh and shank vectors, corresponding to α in Figure 13, was calculated using the dot product:

$$\theta_{\text{included}}(t) = \cos^{-1}\left(\frac{\mathbf{v}_{\text{thigh}}(t)\cdot\mathbf{v}_{\text{shank}}(t)}{\|\mathbf{v}_{\text{thigh}}(t)\|\,\|\mathbf{v}_{\text{shank}}(t)\|}\right).$$

The flexion-style knee-angle proxy, corresponding to β in the schematic, was then defined as:

$$\theta_{\text{knee}}(t) = 180^\circ - \theta_{\text{included}}(t).$$

With this definition, a more extended knee corresponds to a smaller knee-angle proxy, while increased knee flexion corresponds to a larger knee-angle proxy.

E. Time normalization of lift profiles

For every valid lift, the knee-angle trace within the crate-in-air interval was extracted. The trace was then normalized to 101 points, corresponding to 0–100% of the lift. Interpolation was used to map the original time samples onto the normalized lift percentage scale.

This resulted in one normalized knee-angle profile per valid lift:

$$\theta_{\text{knee}}(p),$$

where p represents the normalized lift percentage from 0 to 100%.

F. Participant-level averaging

When multiple valid lifts were available for a participant in the same condition and series, the normalized lift profiles were averaged. This produced one mean normalized knee-angle profile per participant, condition, and series:

$$\overline{\theta}_{\text{knee,participant}}(p).$$

The participant-level profiles were then used for condition-level visualization. This means that the plotted condition-level knee-angle profiles were based on participant averages rather than raw frame-level data.

G. Condition-level comparison

For each load condition, the participant-level knee-angle profiles were grouped by series. The no-exoskeleton and Laevo profiles were then compared visually over the normalized lift cycle. This allowed differences in knee flexion patterns to be inspected across the full lifting movement, rather than reducing the knee angle to only one scalar value.

The same processing workflow was applied to the empty-crate and 5 kg crate conditions. Participants were included only where valid knee-angle profiles were available according to the per-lift validity criterion.

H. Comparison with model knee angle

For comparison with the predictive simulations, the model knee angle was obtained directly from the OpenSim state trajectories. Unlike the experimental knee-angle proxy, which was calculated from hip, knee, and ankle marker positions, the model knee angle was read from the corresponding knee coordinate in the model solution.

The model knee-angle trajectory was normalized to 101 points in the same way as the experimental lift profiles. This allowed the experimental and model knee-angle patterns to be plotted over the same 0–100% normalized lift scale.

It should be noted that the experimental knee angle is a marker-based proxy calculated in the y-z plane, whereas the model knee angle is a generalized coordinate from the OpenSim model. Therefore, the two signals are similar in interpretation, but they are not exactly the same measurement. The comparison should therefore be interpreted as a comparison of knee-flexion patterns rather than a direct validation of identical quantities.

APPENDIX G
OVERVIEW OF THE SETUP OF THE THORACOLUMBAR SPINE MODEL

This appendix gives an overview of the model components retained for the predictive simulations. All coordinate couplers in the original model were kept. Joints that were not required for the sagittal-plane stooping task were locked.

A. Retained joints and actuated coordinates

The retained joints were the left and right hip, knee, ankle, and patellofemoral joints, the ground-pelvis joint, the abdominal joint, and the intervertebral joints from L5/S1 to T12/L1. All other joints were locked.

The actuated coordinates were the left and right hip flexion, hip adduction, hip rotation, knee angle, and ankle angle coordinates, as well as the flexion-extension, lateral-bending, and axial-rotation coordinates of the retained thoracolumbar joints and abdominal joint. The coordinate groups and bounds used in the simulations are summarized in Table VI.

TABLE VI
COORDINATE GROUPS AND BOUNDS USED IN THE PREDICTIVE SIMULATIONS.

Coordinate group	Coordinates	Bounds
Hip flexion	left/right	$[0, 135]^\circ$
Hip adduction	left/right	$[-3, 3]^\circ$
Hip rotation	left/right	$[-3, 3]^\circ$
Knee angle	left/right	$[-16, 10]^\circ$
Ankle angle	left/right	$[-0.1, 0.1]$ rad
Pelvis tilt	pelvis	$[-2, 2]$ rad
Pelvis list	pelvis	$[-3, 3]^\circ$
Pelvis rotation	pelvis	$[-3, 3]^\circ$
Spine FE	L5/S1–T12/L1, Abd	$[-5, 0.3]^\circ$
Spine LB	L5/S1–T12/L1, Abd	$[0, 0]$
Spine AR	L5/S1–T12/L1, Abd	$[0, 0]$

For all listed coordinates, both coordinate-value and coordinate-speed state paths were defined in `inputfile_forwardbend.py`. In the final setup, no active speed targets were used, because the speed-target blocks were commented out. No active final-value targets were set for these states.

B. Removed actuators

The original actuators related to the arms and shoulders were removed, since arm motion was not part of the simulated stooping task. The removed actuators were:

- `elbow_L_actuator`, `elbow_R_actuator`;
- `shoulder_elv_l_actuator`, `shoulder_rot_l_actuator`, `elv_angle_l_actuator`;
- `shoulder_elv_r_actuator`, `shoulder_rot_r_actuator`, `elv_angle_r_actuator`.

C. Muscles retained for the hip and leg simulations

For the hip and leg muscle simulations, a reduced bilateral muscle set was retained, visible in Figure 14. This set included hip flexors, hip extensors, hip abductors, knee flexors, knee extensors, and selected ankle-related muscles. The retained muscles were:

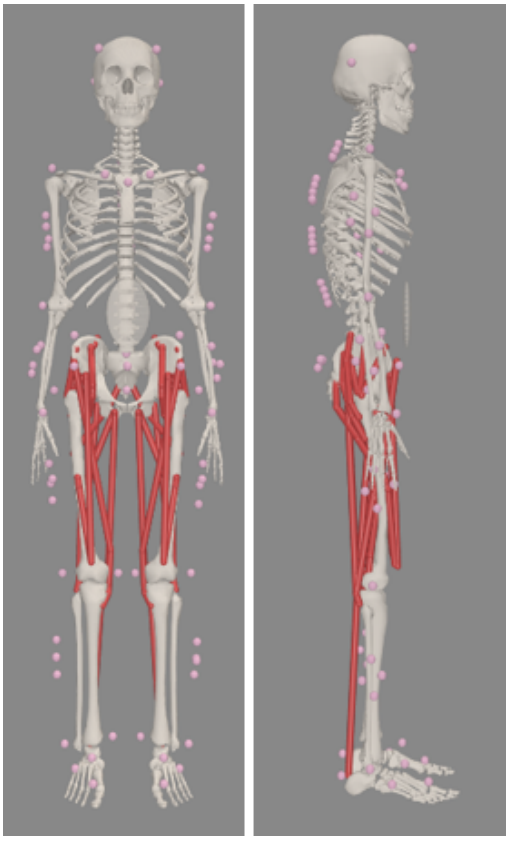

Fig. 14. A screenshot from OpenSim, showing the model with all muscles included for the hip and leg simulations.

- `iliacus_r`, `iliacus_l`;
- `glut_max1_r`, `glut_max2_r`, `glut_max3_r`;
- `glut_max1_l`, `glut_max2_l`, `glut_max3_l`;
- `glut_med1_r`, `glut_med2_r`, `glut_med3_r`;
- `glut_med1_l`, `glut_med2_l`, `glut_med3_l`;
- `rect_fem_r`, `rect_fem_l`;
- `bifemlh_r`, `bifemsh_r`, `bifemlh_l`, `bifemsh_l`;
- `add_mag2_r`, `add_mag2_l`;
- `grac_r`, `grac_l`;
- `med_gas_r`, `med_gas_l`;
- `sar_r`, `sar_l`;
- `vas_int_r`, `vas_int_l`.

D. Muscles retained for the back-muscle simulations

For the back-muscle simulations, a reduced set of thoracolumbar extensor muscles was retained, see Figure 15. This set consisted of the longissimus thoracis pars lumborum and iliocostalis lumborum muscle paths on both sides of the model:

- `LTpL_L1_r`, `LTpL_L2_r`, `LTpL_L3_r`, `LTpL_L4_r`, `LTpL_L5_r`;
- `LTpL_L1_l`, `LTpL_L2_l`, `LTpL_L3_l`, `LTpL_L4_l`, `LTpL_L5_l`;
- `IL_L1_r`, `IL_L2_r`, `IL_L3_r`, `IL_L4_r`;

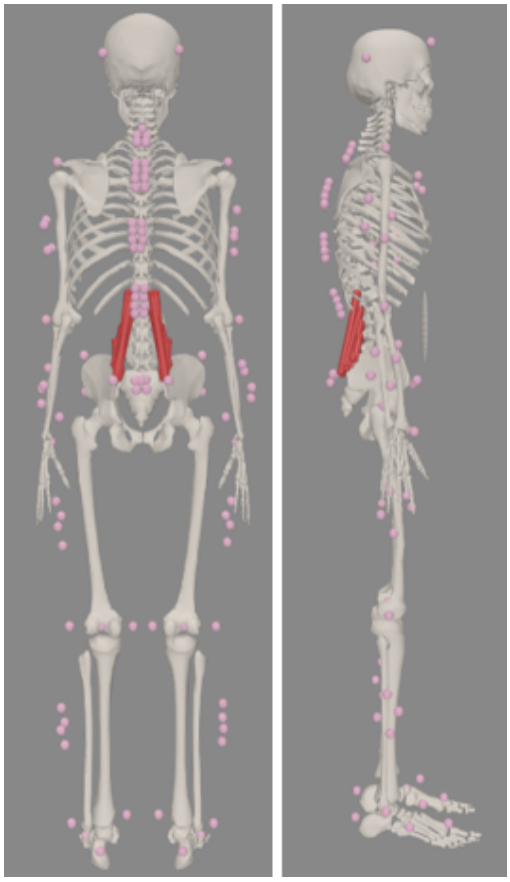

Fig. 15. A screenshot from OpenSim, showing the model with all muscles included in the back-muscle simulations.

- `IL_L1_l`, `IL_L2_l`, `IL_L3_l`, `IL_L4_l`.

Because this back-muscle set did not actuate all retained spinal levels equally, reserve actuators were still required in the back-muscle simulations. This limitation is discussed in the main text.

APPENDIX H
LAEVO MEASUREMENTS AND DERIVATION OF ANGLE-TORQUE RELATIONSHIP

A. Background and goal of the measurements

To model the Laevo, the relationship between exoskeleton configuration and support torque had to be determined. The Laevo is a rigid passive back-support exoskeleton in which the angle between the thigh and trunk influences the amount of support. However, the exact angle-torque relationship was not available in a form suitable for modelling. Therefore, measurements were performed to derive this relationship experimentally.

B. Measurement setup

To measure the angle-force relationship, a test setup with a mechanical dummy was used, a schematic drawing can be found in Figure 2. The dummy consisted of 3D-printed elements shaped to represent a human torso and upper legs. This allowed the Laevo to be mounted on the dummy in a similar way as it would be mounted on a human, for instructions see Appendix D. The trunk of the dummy was rigid and had one rotational degree of freedom, corresponding to hip flexion. Separate weights of 25 kg were used to represent the mass of the dummy trunk.

A pulley was connected below the torso and leg elements. A cable ran over this pulley, with one side connected to the weights and the other side connected to a tensile testing machine. The tensile testing machine was configured such that upward motion of the machine corresponded to stooping motion of the dummy. The force measured by the tensile testing machine was converted into a torque using the pulley radius.

In addition to the tensile testing machine, an Arduino-based measurement system was present in the setup. This system included a compression sensor mounted at approximately the L5/S1 level and a button that was activated when the dummy was pulled to its lowest position. The compression-sensor data were not used in the final derivation of the angle-torque relationship in this thesis, but the Arduino system is mentioned here because it formed part of the original measurement setup.

C. Testing procedure

The tensile testing machine was programmed to follow a fixed motion sequence so that the relevant loading cycle could be identified consistently and, when needed, synchronized with the Arduino measurements. A schematic drawing of the programmed motion can be found in Figure 16. Starting from a resting position, the machine first moved to a reference position at which a button connected to the Arduino was pressed. It then moved through the main test trajectory until the dummy reached the prescribed maximum flexion, after which it returned to the reference position and finally moved back to rest. In this setup, upward motion of the tensile testing machine corresponded to stooping motion of the dummy through the pulley-cable system. The button press was used as a timing marker for synchronization of the Arduino recordings.

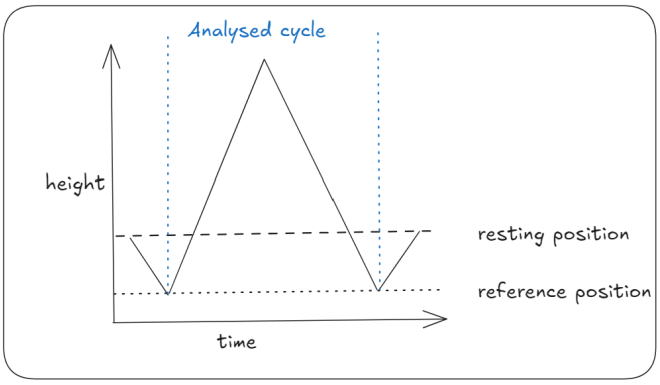

Fig. 16. Schematic drawing of the tensile testing machine movement during the Laevo measurement procedure. The programmed movement included a reference position for synchronization and a main loading-unloading cycle used to derive the angle-torque relationship. This ensured that the analysed cycle corresponded to the relevant flexion and return motion of the dummy-Laevo system.

For the measurements considered in this thesis, tests were performed under two conditions: a gravity-only condition without the exoskeleton and a condition with the Laevo in the medium support setting. Each condition was repeated multiple times to assess repeatability and to allow averaging across runs. In the dataset used for the present analysis, eight gravity-only runs and ten Laevo medium-setting runs were available.

D. Recorded data

The measurement setup produced two data streams: a tensile-machine log and an Arduino log. The tensile-machine log contained the measured pulling force together with the machine displacement. In the files used here, each row consisted of three numeric values, interpreted in the analysis as force, relative displacement, and absolute position. The force measurement was used to derive the support torque through the pulley radius, while the relative displacement was used to determine the corresponding rotation angle of the dummy-exoskeleton system. The absolute position was not used.

The Arduino log contained measurements from the compression sensor together with timing information. Force samples were stored together with timestamps, and button-trigger events were stored as separate timing markers. These timing markers were intended to allow synchronization between the Arduino and tensile-machine recordings. In the present thesis, the Arduino compression measurements were not used in the final derivation of the Laevo relationship, but they are included here for completeness because they formed part of the original measurement setup.

E. Pairing the tensile and Arduino logs

To start the analysis, the tensile-machine and Arduino log files were grouped into measurement runs. For the regular exoskeleton measurements, this pairing was based on the run identifier contained in the filenames. In this way, the tensile-machine log and the Arduino log belonging to the same trial could be matched before further processing. The

analysis script searched the filenames for both the exoskeleton condition and the run number, and used this information to create corresponding file pairs.

For the gravity-only measurements, the filename structure differed slightly between the tensile-machine and Arduino recordings. In those cases, gravity files were first identified separately, after which the Arduino files were matched to the closest tensile-machine file based on file modification time. This ensured that the corresponding gravity measurements could also be linked for analysis.

F. Converting the data into angle and torque

After the files were paired, the tensile-machine data were converted into the mechanical quantities needed for further analysis. The measured tensile force was used to determine the torque applied about the pulley, while the measured displacement was used to estimate the corresponding rotation angle of the dummy-exoskeleton system. In the raw tensile-machine files, the analysis used the measured force together with the recorded relative displacement.

Before converting the displacement into an angle, a force-dependent correction was applied to the measured relative displacement:

$$r_{\mathrm{corr}} = r_{\mathrm{rel}} - Fk, \tag{7}$$

where r_{corr} is the corrected relative displacement, r_{rel} is the measured relative displacement, F is the measured tensile force, and k is a small correction factor used in the analysis. In the script, this factor was defined as

$$k = \frac{0.001}{1000}. \tag{8}$$

The corrected displacement was then converted into a rotation angle using the pulley geometry. First, the pulley circumference was defined as

$$C = 2\pi R, \tag{9}$$

with R the pulley radius. The displacement-to-angle conversion factor was then given by

$$c = \frac{2\pi}{1000\,C}, \tag{10}$$

so that the rotation angle β could be written as

$$\beta = r_{\mathrm{corr}} c. \tag{11}$$

Since $C = 2\pi R$, this is equivalent to

$$\beta = \frac{r_{\mathrm{corr}}}{1000\,R}. \tag{12}$$

The tensile force was converted into torque about the pulley according to

$$M = FR, \tag{13}$$

where M is the torque and R is the pulley radius. In the analysis, the pulley radius was taken as

$$R = 0.070 \text{ m}. \tag{14}$$

Using these steps, each sample in the tensile-machine log was transformed from a force-displacement measurement into a corresponding angle-torque data point. These angle-torque data were then used as the basis for the subsequent cycle selection and averaging steps.

G. Selecting the analysed cycle

After the tensile-machine data had been converted into angle-torque data, one complete motion cycle was selected from each run for further analysis. The programmed machine motion contained multiple phases, including movement to and from the reference position used for synchronization. For the derivation of the Laevo relationship, only the main loading-unloading cycle was used, see Figure 16. In the analysis script, this cycle was identified from the corrected displacement signal by detecting a sequence consisting of a local minimum, followed by a local maximum, and then the next local minimum.

The selected segment therefore represented one complete flexion and return movement of the dummy. After this cycle had been identified, the first minimum of the selected segment was used as the zero reference for the angle. As a result, the analysis was based on a relative angle definition rather than on an absolute anatomical angle.

H. Separating loading and unloading

After the analysed cycle had been selected, it was separated into loading and unloading branches. In physical terms, the loading branch corresponded to the stooping movement of the dummy, while the unloading branch corresponded to the return movement. This separation was necessary because the angle-torque behaviour was assumed to not be identical in both directions. Instead, hysteresis was expected, meaning that the torque at a given angle could differ between loading and unloading.

The maximum angle of the selected cycle was used as the transition point between the loading and unloading branches. The two branches were then retained and analysed separately throughout the subsequent processing steps. This allowed the final measured behaviour of the Laevo to be represented as distinct loading and unloading curves rather than as a single angle-torque relationship.

If the Arduino compression measurements were included, they were synchronized to the selected machine cycle using the recorded timing markers from the button presses. In that case, the Arduino samples belonging to the same cycle could be mapped onto the corresponding angle range of the tensile-machine data. These compression measurements were not used in the final angle-torque relationship.

I. Aligning repeated runs to a common angle axis

After the loading and unloading branches had been identified for each run, the runs were aligned to a common angle axis. This was necessary because the measured runs did not contain data points at exactly the same angle values and did not always cover exactly the same angle range. To allow comparison and averaging across runs, the angle-torque data were therefore interpolated onto a common angle grid.

This common grid was constructed from the angle ranges present in the measured runs. The loading and unloading branches of each run were then interpolated separately onto this grid. As a result, torque values from different runs could be compared at the same angle values in the later averaging steps.

J. Constructing the gravity baseline

The gravity-only measurements were processed in the same way as the Laevo measurements. For each gravity run, the machine data were converted into angle-torque data, the analysed cycle was selected, and the loading and unloading branches were identified. These gravity curves were then aligned to the same common angle axis as the Laevo runs.

After alignment, the gravity-only runs were combined to obtain representative loading and unloading gravity curves. These curves represented the contribution of the dummy and test setup without the Laevo. They were used as a baseline in the next step of the analysis.

K. Isolating the Laevo contribution

To isolate the contribution of the Laevo itself, the gravity baseline was subtracted from the measured Laevo runs. This was done separately for the loading and unloading branches after interpolation to the common angle axis. The resulting curves represented the measured angle-torque behaviour of the Laevo with the contribution of the dummy and test setup removed.

In this way, the processed Laevo curves can be interpreted as the support provided by the exoskeleton itself, rather than the combined response of the full measurement setup.

L. Averaging and outlier handling

After gravity correction, the repeated Laevo runs were compared and combined into representative curves. Because repeated measurements can differ slightly, an outlier detection step was included in the analysis. Runs that deviated strongly from the overall group could therefore be identified before calculating the final representative relationship.

After this, the corrected loading and unloading curves were averaged across runs. This produced one representative loading curve and one representative unloading curve for the Laevo. These averaged curves formed the main result of the measurement analysis.

M. Final relationship used for modelling

The final output of the analysis was a processed angle-torque relationship for the Laevo, represented by separate loading and unloading curves. These curves described the support moment provided by the exoskeleton as a function of the measured flexion angle. The separate branches were retained for the OpenSim implementation, where the loading branch was used for the stooping simulation and the unloading branch was used for the standing-up simulation.

APPENDIX I
ADDING THE LAEVO TO OPENSIM

A. Expression based coordinate force

To represent the support provided by the Laevo in OpenSim, an `ExpressionBasedCoordinateForce` was added to the hip flexion coordinate. This force type allows the generalized moment about a coordinate to be defined as an explicit analytical expression of the coordinate value. It was chosen because the Laevo support had been derived experimentally as an angle-dependent torque relationship, which could therefore be implemented directly as a passive coordinate-dependent moment.

The measured relationship obtained in the previous section showed hysteresis (see Figure 3, meaning that the torque-angle behaviour differed between stooping and standing up. In the present work, the stooping and standing-up motions were simulated separately. For this reason, two separate OpenSim implementations were created: one using the loading branch of the measured curve for the stooping motion, and one using the unloading branch for the standing-up motion. In this way, the measured hysteretic behaviour could be retained without introducing a switching rule within a single simulation.

The measurements were performed on the complete Laevo device, while the OpenSim model contains separate left and right hip flexion coordinates, each of which got its own expression based coordinate force added. The measured angle-torque relationship was therefore interpreted as the total support of the bilateral exoskeleton. To represent this in the model, the measured torque was divided equally over the left and right hip coordinate forces. As a result, the sum of the left and right exoskeleton moments in the OpenSim model corresponded to the measured whole-device support.

B. Fit

The measured loading and unloading branches could not be inserted into the `ExpressionBasedCoordinateForce` directly as discrete data points, because this force component requires a continuous fitted expression. Therefore, each branch was approximated by a fitted expression that could be evaluated directly by OpenSim. For this purpose, a piecewise linear spline representation was used, written as a sum of hinge functions. This form was chosen because it provides a flexible but still interpretable approximation of the measured curve and can capture the observed nonlinear behaviour without requiring a high-order global polynomial.

To obtain fitted expressions that could be used robustly in OpenSim and OpenSim Moco, the piecewise linear spline was implemented in a smoothed form. Without smoothing, the hinge representation would likely introduce sharp changes in the derivative of the torque-angle relation at the knot locations, which may lead to less favourable numerical behaviour during simulation and optimization. Separate fitted expressions were generated for the loading and unloading branches because the measured Laevo behaviour showed hysteresis, meaning that the torque-angle relationship differed between stooping and standing up. Since these motions were simulated separately in the present work, representing them with separate fitted expressions was considered more appropriate than forcing both branches into a single averaged relation.

The complexity of each fitted expression was controlled through the number of interior knots. In the present implementation, the number of interior knots was varied between 6 and 18, and the smallest number that reduced the root-mean-square error below 0.30 Nm was selected. This provided an objective selection rule and balanced accurate representation of the measured data against unnecessary increase in fit complexity.

Before fitting, negative torque values near the branch boundaries were clipped to zero. These negative values are not interpreted as physical support provided by the exoskeleton itself, but as an artefact of the force calculation procedure used in the original company analysis pipeline. Clipping was therefore applied to prevent these boundary artefacts from being incorporated directly into the fitted OpenSim force law.

TABLE VII
COEFFICIENTS AND KNOT LOCATIONS USED FOR THE SMOOTHED PIECEWISE LINEAR LAEVO TORQUE EXPRESSIONS IN EQUATION 1.

Down branch			Up branch		
Term	Coeff.	Knot	Term	Coeff.	Knot
a_0	-1.02986	–	a_0	-0.415257	–
a_1	50.6671	–	a_1	10.1246	–
a_2	35.9673	0.132914	a_2	50.6842	0.116937
a_3	-5.74993	0.257100	a_3	-0.765614	0.225147
a_4	-5.42965	0.381287	a_4	8.45339	0.333358
a_5	-32.8914	0.505474	a_5	-33.2505	0.441568
a_6	-19.6053	0.629661	a_6	-24.1046	0.549779
a_7	-16.7444	0.753848	a_7	-5.00981	0.657989
a_8	-6.64217	0.878035	a_8	-2.60630	0.766200
a_9	-0.415740	1.00222	a_9	-7.79461	0.874410
a_{10}	-7.74071	1.12641	a_{10}	-0.918945	0.982620
a_{11}	12.3280	1.25060	a_{11}	2.98703	1.09083
a_{12}	-6.23352	1.37478	a_{12}	3.16775	1.19904
a_{13}	-11.2167	1.49897	a_{13}	-1.85632	1.30725
			a_{14}	-13.4480	1.41546
			a_{15}	141.704	1.52367

Figure 3 shows the measured loading and unloading branches together with the fitted expressions. The fitted expressions followed the smoothed piecewise linear form given in Equation 1, and the corresponding coefficients and knot locations are listed in Table VII. For the loading branch, the final fit used 12 interior knots and resulted in an RMSE of 0.255 Nm, a mean absolute error of 0.184 Nm, and a maximum absolute error of 1.150 Nm. For the unloading branch, the final fit used 14 interior knots and resulted in an RMSE of 0.225 Nm, a mean absolute error of 0.167 Nm, and a maximum absolute error of 0.966 Nm. These errors were considered sufficiently small relative to the measured torque magnitudes, and the fitted expressions were therefore used as the final OpenSim representation of the Laevo support.

The unloading branch shows a pronounced end-range feature coming from hysteresis that is preserved in the fitted expression because it is present in the processed measured branch obtained from the analysis pipeline. In the present simulations, however, this feature is expected to have little practical influence, because it occurs only at hip flexion angles above approximately (80°), whereas the simulated motions considered here remain below this range, with maximum an-

gles only slightly above 1 rad, corresponding to approximately ($60°$). It was therefore retained to remain consistent with the processed measurement data, while not being expected to substantially affect the model behaviour in the simulated motions. This does mean that the current implementation does not reproduce hysteresis caused by changes in movement direction within a single simulation, but this was considered outside the scope of this thesis.

The resulting fitted expressions were then assigned to `ExpressionBasedCoordinateForce` components acting on the left and right hip flexion coordinates. Two bilateral OpenSim models were created: one for stooping, based on the loading branch, and one for standing up, based on the unloading branch.

APPENDIX J
AI DECLARATION

Artificial intelligence (AI) tools were used during this thesis. They were used in two ways. First, AI was used as support during coding, mainly to write and debug scripts more quickly. All code written with AI support was checked before use, either by reading the code or by checking the resulting graphs, outputs, and data-processing steps.

Second, AI was used as writing support, mainly to improve flow, word choice, grammar, and clarity. The scientific content, interpretation of the results, and final decisions remained my own responsibility. All AI-assisted text was read, edited where needed, and approved before being included in the thesis.